Magma Evolution and Open-System Processes at Shiveluch Volcano: Insights from Phenocryst Zoning

MADELEINE C. S. HUMPHREYS*, JON D. BLUNDY AND R. STEPHEN J. SPARKS

DEPARTMENT OF EARTH SCIENCES, UNIVERSITY OF BRISTOL, WILLS MEMORIAL BUILDING, QUEEN'S ROAD, BRISTOL BS8 1RJ, UK

Phenocryst zoning patterns are used to identify open-system magmatic processes in the products of the 2001 eruption of Shiveluch Volcano, Kamchatka. The lavas and pumices studied are hornblende–plagioclase andesites with average pre-eruptive temperatures of $\sim 840^{\circ}C$ and fO_2 of 1·5–2·1 log units above nickel–nickel oxide (NNO). Plagioclase zoning includes oscillatory and patchy zonation and sieve textures. Hornblendes are commonly unzoned, but some show simple, multiple or patchy zoning. Apatite microphenocrysts display normal and reverse zoning of sulphur. The textural similarity of patchy hornblende and plagioclase, together with Ba–Sr systematics in patchy plagioclase, indicate that the cores of these crystals were derived from cumulate material. Plagioclase–liquid equilibria suggest that the patchy texture develops by resorption during H_2O-undersaturated decompression. When H_2O-saturated crystallization recommences at lower pressure, reduced pH_2O results in lower X_{An} in plagioclase, causing more Al-rich hornblende to crystallize. Plagioclase cores with diffuse oscillatory zoning, and unzoned hornblende crystals, probably represent a population of crystals resident in the magma chamber for long periods of time. In contrast, oscillatory zoning in the rims of plagioclase phenocrysts may reflect eruption dynamics during decompression crystallization. Increasing Fe/Al in oscillatory zoned rims suggests oxidation as a result of degassing of H_2O during decompression. A general lack of textural overlap between phenocryst types suggests that different phenocryst populations were spatially or temporally isolated during crystallization. We present evidence that the host andesite has mixed with both more felsic and more mafic magmas. Olivine and orthopyroxene xenocrysts with reaction or overgrowth rims and strong normal zoning indicate mixing with basalt. Sieve-textured plagioclase resulted from mixing of a more felsic magma with the host andesite. The mineralogy and mineral compositions of a mafic andesite enclave are identical to those of the host magma, which implies efficient thermal quenching, and thus small volumes of intruding magma. Mixing of this magma with the host andesite results in phenocryst zoning because of differences in dissolved volatile contents. We suggest that small magma pulses differentiated at depth and ascended intermittently into the growing magma chamber, producing incremental variations in whole-rock compositions.

KEY WORDS: patchy zoning; magma mixing; Shiveluch

INTRODUCTION

Open-system magmatic processes are ubiquitous phenomena at island arc volcanoes. Processes may include segregation and ascent of magmas from depth, accumulation and mixing of magma batches in a shallow chamber, and eruptive processes. The intricacy of the magmatic history is reflected to varying extents in the typically complex petrography of erupted andesites. Eruptive products thus contain clues to the entire magma history, from differentiation in the deep crust to eruption at the surface.

Magma mixing phenomena are particularly widespread (e.g. Anderson, 1976; Eichelberger, 1980; Clynne, 1999). Mixing is envisaged to occur in various scenarios: for example, thermal or chemical convection in a magma chamber (e.g. Huppert et al., 1982; Couch

*Corresponding author. Present address: Department of Earth Sciences, University of Cambridge, Downing Street, Cambridge CB2 3EQ, UK. Telephone: 0122 376 5260. Fax: 0122 333 3450. E-mail: mcsh2@cam.ac.uk

et al., 2001), within the conduit during eruption (Snyder & Tait, 1996; Koyaguchi, 1985) or during sidewall crystallization in mafic magma chambers (McBirney, 1980). Mixing can also occur as a result of recharge of the magma chamber by the arrival of a new magma batch, which may be a trigger for eruptions (e.g. Sparks *et al.*, 1977; Huppert *et al.*, 1982; Murphy *et al.*, 1998). Magma recharge commonly occurs as cool, silicic melt is invaded by hotter, more mafic magma (e.g. Anderson, 1976; Clynne, 1999; Murphy *et al.*, 2000). This process is typically inferred from features such as the presence of mafic enclaves, accompanied by heavily corroded xenocrysts and significant geochemical zonation in phenocrysts (Eichelberger, 1978, 1980). The reverse process (i.e. injection of more silicic magma into basaltic systems) has also been inferred on the basis of field observations (Wiebe, 1987) and geochemistry (Calanchi *et al.*, 1993). Less attention has been paid to the possibility of 'cryptic' magma mixing, which we define here as the repeated mixing of small pulses of magma that have similar anhydrous bulk compositions, but may have different fO_2 or volatile contents. Magma recharge would be difficult to detect if the mixing magmas were compositionally similar, because of limited disequilibrium between crystals and melt (D'Lemos, 1996).

Recently, field evidence has shown that plutons can grow incrementally via the coalescence of many much smaller magma bodies (Bateman, 1992; John & Blundy, 1993; Wiebe & Collins, 1998; Atherton, 1999; Glazner *et al.*, 2004). This implies that some subvolcanic magma chambers are built up gradually and over prolonged periods of time from many small batches of magma. The magma batches may have differentiated at depth prior to ascent (Annen *et al.*, 2006) and been injected into a shallow-level magma chamber. The efficiency of magma mixing resulting from such recharge depends on the volume ratio of intruding magma to resident magma, and on the viscosity contrast between the two magmas (e.g. Sparks & Marshall, 1986; Jellinek *et al.*, 1999). This in turn depends on the relative temperatures, dissolved volatile contents and compositions of the magmas (Sparks & Marshall, 1986). If the intruding magma forms enclaves, enclave mineralogy will depend on the rate of quenching as well as the bulk composition of the intruding magma (Blundy & Sparks, 1992). Further fragmentation or disaggregation of enclaves can help to hybridize the mixed magma (Clynne, 1999, and references therein). The resulting mineral textures will depend on how close the enclave mineralogy is to equilibrium with the host magma, and thus on the composition and relative volume of the intruding magma.

As well as recharge and mixing, other processes that contribute to the textural complexity of andesites include the resorption and remobilization of earlier-formed crystals or cumulate materials, as magma ascends from its deep source to a shallow magma storage area (Pyle *et al.*, 1988; Turner *et al.*, 2003; Dungan & Davidson, 2004). In the storage area, the magma may slowly cool and degas, promoting crystal fractionation. Convection in a zoned magma can cause compositional zoning in existing phenocrysts (Singer *et al.*, 1995). Late-stage crystal growth may occur during magma ascent in the conduit, in response to depressurization and degassing of H_2O (e.g. Geschwind & Rutherford, 1995).

In this paper we investigate phenocryst zoning in andesitic dome rocks and pumices from Shiveluch Volcano, Kamchatka, with the aim of identifying different magmatic processes through their effects on the phenocrysts. We identify different populations of phenocrysts based on their textural and geochemical characteristics, and attempt to produce an integrated picture of magmatic processes in their spatial and temporal context. We show that the host andesite has mixed with basalt, producing xenocrysts showing significant disequilibrium textures. The host andesite has also mixed with a mafic andesite, although efficient quenching resulted in cryptic mixing, with identical mineralogy and mineral compositions in both the enclave and the host andesite. Geochemical zonation is produced in crystals from both magmas as a consequence of variations in volatile contents between the magmas. We also discuss the remobilization of cumulates, and the effects of decompression and eruption dynamics on the evolution of the magma at both deep and shallow levels, thus revealing a complex record of open-system processes at this active andesite volcano.

GEOLOGICAL BACKGROUND

Shiveluch Volcano is located in the northern Central Depression of the Kamchatka Peninsula (Fig. 1), and has been one of the most active andesitic volcanoes in the Kamchatka–Kurile arc during the Holocene, with at least 60 tephra fall deposits identified, marking explosive eruptions with volumes in excess of 0·1 km^3 (Dirksen *et al.*, 2006). It has a compound edifice, comprising sections from two distinct episodes of activity. Old Shiveluch is the remains of a basalt to basaltic andesite stratovolcano (Menyailov, 1955; Melekestsev *et al.*, 1991). The southern section of this edifice was destroyed by a huge landslide during the late Pleistocene (Melekestsev *et al.*, 1991), producing a 9 km wide caldera that exposes NE-trending, basaltic andesite dykes within the cone (Belousov *et al.*, 1999). The younger edifice, Molody Shiveluch, has been growing throughout the Holocene. Eruptive activity at Molody Shiveluch is typified by Plinian eruptions alternating with dome-building and phreatic activity (Belousov *et al.*, 1999).
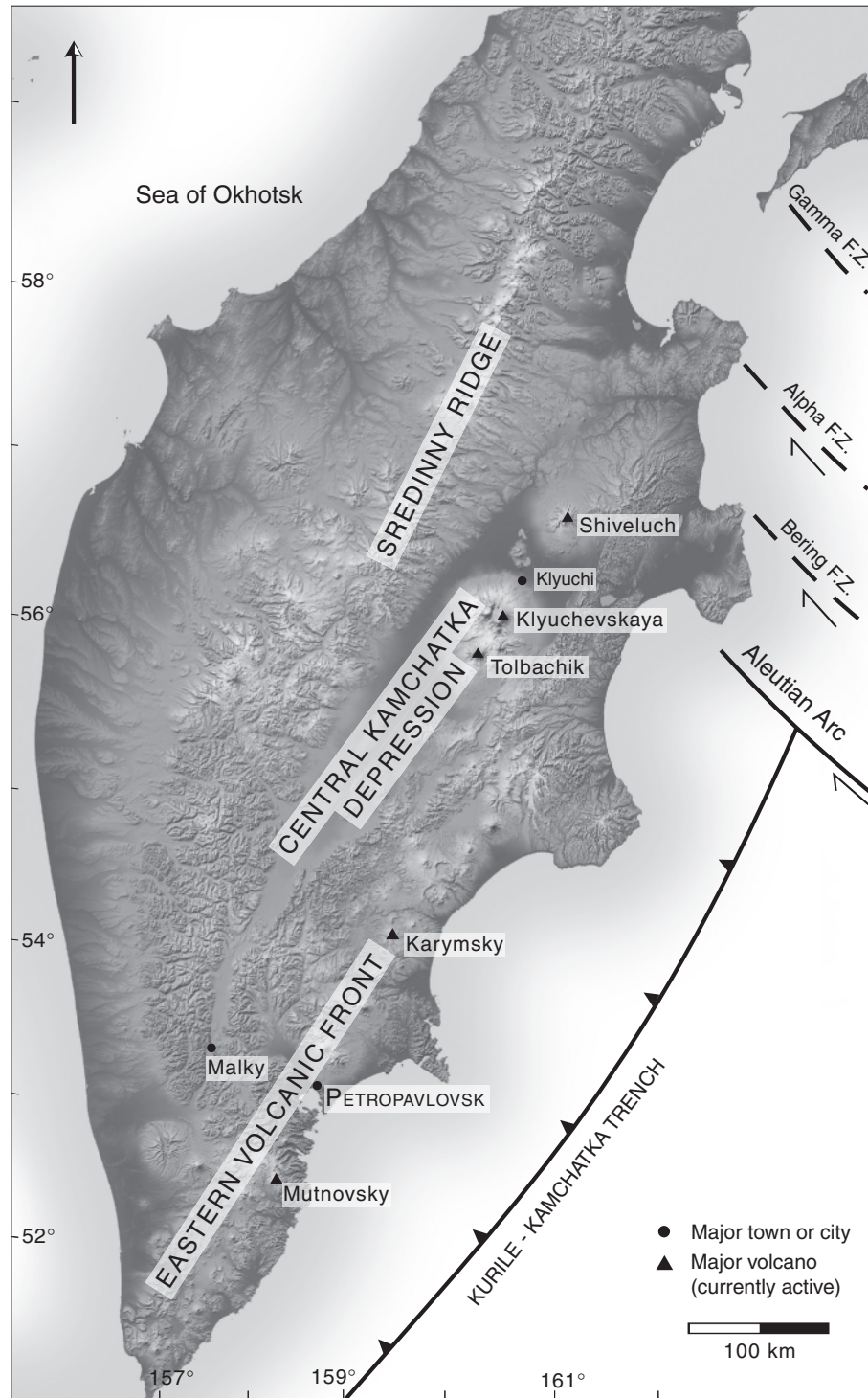
Fig. 1. Regional map of the Kamchatka Peninsula, showing subduction zones, regions of magmatism and some major active volcanoes. Magmatism is split into the Eastern Volcanic Front, Sredinny Ridge (currently inactive) and the Central Kamchatka Depression. The region north of the Aleutian trench is split by fracture zones and magnetic lineations, indicating an extinct trench trending to the NE (Baranov *et al.*, 1991; Portnyagin *et al.*, 2005). The convergence of the Pacific plate with the Aleutian arc is oblique; the angle of convergence increases eastward (Geist & Scholl, 1994). Shaded topographic base map is taken from NASA Earth Observatory.

Juvenile material is predominantly amphibole–plagioclase andesite (Melekestsev et al., 1991).

The most recent phase of volcanic activity started in 1964 with a strong Plinian eruption triggered by edifice failure (Belousov, 1995). This was followed by episodes of dome extrusion in 1980–1981, 1993–1995 and 2001–2004. These periods of active extrusion were separated by less intense activity (e.g. Firstov et al., 1994; Zharinov et al., 1995; Dirksen et al., 2006). In this study we focus on rocks erupted during the most recent extrusive episode, 2001–2004.

Summary of andesite petrology

We studied samples of dome rock, and pumiceous material taken from pyroclastic flows, from early in the 2001–2004 eruption of Shiveluch Volcano (Table 1). The petrology of the andesite has been described by Dirksen et al. (2006), including whole-rock and modal data, and is summarized and extended here. The main phenocrysts ($>300\ \mu m$) and microphenocrysts ($100–300\ \mu m$) are plagioclase (56–70% of phenocrysts), hornblende (27–35%), Fe–Ti oxides (1·7–4·8%) and orthopyroxene (0·3–5·2%). Clinopyroxene, apatite and anhydrite are present in minor amounts. Quartz and other silica phases are absent. Xenocrysts of olivine and orthopyroxene are present. The groundmass comprises a rhyolitic glass with microlites of plagioclase, clinopyroxene, orthopyroxene and Fe–Ti oxides. Total phenocryst contents vary from $\sim26\%$ (pumices) to $\sim52\%$ (dome rocks), calculated vesicle-free.

Plagioclase compositions range from An_{29} to An_{74}; microlite compositions range from An_{44} to An_{51}. Plagioclase phenocrysts commonly contain inclusions of Fe–Ti oxides, hornblende, apatite and glass. Orthopyroxene and clinopyroxene inclusions occur less commonly; phlogopite, bornite and anhydrite inclusions occur rarely. Hornblende compositions range from Mg-number $[100 \times Mg/(Mg + Fe_{tot})]$ of 58 to 81, classifying as magnesio-hornblendes (Leake, 1978). Hornblende phenocrysts commonly contain inclusions of plagioclase, Fe–Ti oxides, apatite and glass, with rare pyroxene, anhydrite, phlogopite and bornite inclusions. Small, rounded hornblende is present in the groundmass of some samples. Orthopyroxene phenocrysts and microphenocrysts vary in composition from En_{66} to En_{73}, and may contain inclusions of Fe–Ti oxides and apatite. Groundmass orthopyroxene compositions are typically $En_{70–74}$. Orthopyroxene in reaction rims on olivine xenocrysts, in crystal clots or included in olivine is more Mg-rich ($En_{74–87}$). Orthopyroxene xenocrysts, identified by strong normal zoning and a hornblende rim, have high Mg (En_{89}), Cr and Fe^{3+}/Fe^{2+} [calculated using Lindsley (1983)] in the core, decreasing towards the rim (En_{75}). Clinopyroxene is occasionally included in the cores of phenocrysts, occurs rarely as large, anhedral crystals, and commonly in the groundmass. Clinopyroxene compositions range from Wo_{40} to Wo_{44}. Fe–Ti oxides occur as microphenocrysts and microlites, as inclusions in phenocrysts and as symplectites in the breakdown of olivine. Fe–Ti oxides are dominated by spinels (2·7–8·5 wt % TiO_2), with minor ilmenite (28 wt % TiO_2).

Accessory minerals in the andesites studied include apatite and rare anhydrite as primary microphenocrysts, and anhedral Cu–Fe sulphides, cassiterite (SnO_2) and CuO in the groundmass and as inclusions in plagioclase and hornblende. The copper-bearing sulphide is a solid solution of bornite and digenite, ranging from Cu_8FeS_3 to $Cu_{47}FeS_{14}$. Apatite contains up to 5860 ppm sulphur, and is ubiquitous in the rocks studied.

Melt inclusions are common in both hornblende and plagioclase (Humphreys, 2006). Bubbles are common; partial devitrification or precipitation of daughter phases is common in hornblende-hosted inclusions but rare in plagioclase-hosted inclusions. Analysis of melt inclusions containing daughter minerals was avoided where
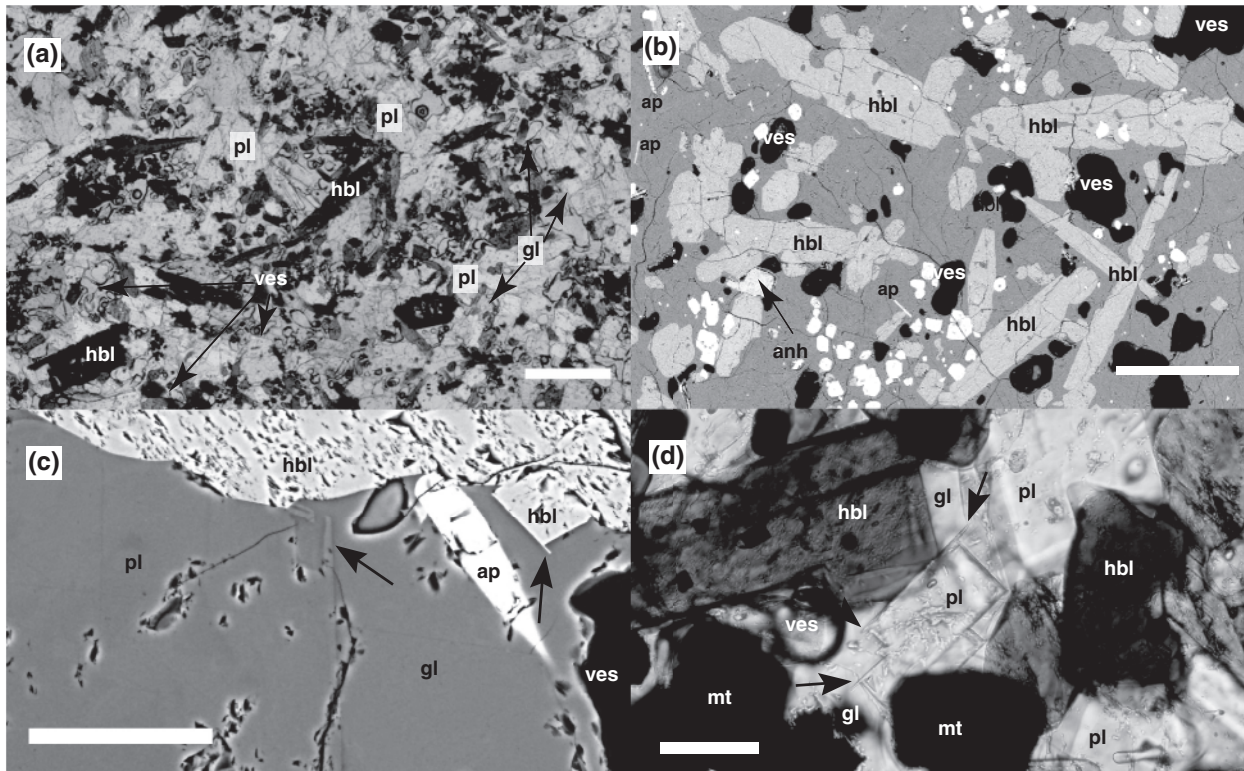
Table 1: Names and descriptions of samples studied

Sample name	Date collected	Description
SHIV01/#1	May 2001	Material from initial block-and-ash flows in period 2–18 May 2001.
		Probably represents the first portion of fresh lava. Dense, slightly vesiculated andesite. Slight alignment of vesicles and phenocrysts
SHIV01/#2	19 May 2001	Pumiceous material from pyroclastic flows erupted during strongly explosive episode. Pale-grey, friable andesite. Elongate vesicles faintly aligned
SHIV01/#3	July 2001	Material from block-and-ash flows produced during dome-building.
		Abundant phenocrysts; faint alignment of elongate hbl and vesicles.
		Contains quenched enclave
SHIV01/#4	May 2001	Pumiceous material taken from pyroclastic flows. Low density, pale, veisculated material
SHV202002	July 2002	Material taken directly from dome carapace. Dense, slightly vesiculated andesite
SHV202003	May 2001	Pumiceous material from pyroclastic flows produced during May 2001.
		Pale grey, vesicular andesite, Relatively crystal-poor

Fig. 2. Petrographic features of the quenched enclave. Photomicrograph (a) shows elongate, skeletal hornblende (hbl) phenocrysts and plagioclase (pl) in vesicle-rich glass (scale bar represents 1 mm). Back-scattered SEM photograph (b) shows abundant, acicular apatite (ap), anhydrite (anh) and elongate hornblende (scale bar represents 500 μm). Tabular white minerals are titanomagnetite (mt). It should be noted that plagioclase and glass (gl) are indistinguishable in this image. Dendritic extensions (indicated by arrows) on plagioclase and hornblende crystals (c, d) indicate rapid growth. Scale bar in (c) represents 50 μm (c), and in (d) 100 μm.

possible. Because there is little compositional difference between inclusions in different host phenocrysts, or between inclusions with and without bubbles (Humphreys, 2006), we assume that post-entrapment crystallization is limited, and that the inclusions accurately reflect the composition of the melt at the time of trapping. Detailed melt inclusion data have been given by Humphreys (2006) and the results are summarized here. Melt inclusions are consistently rhyolitic in composition, containing 70–80 wt % SiO_2 (normalized to anhydrous) and 0·1–5·1 wt % H_2O as analysed by secondary ionization mass spectrometry (SIMS). Matrix glasses are among the most silica-rich, typically containing 77·5–79·5 wt % SiO_2, and low H_2O (0·10–0·14 wt %). H_2O correlates negatively with SiO_2 content of the inclusions, and the inclusions follow a decompression trend on the Qz–Or–Ab ternary.

The andesites contain dark green, medium- to coarse-grained xenoliths. These are typically several centimetres in diameter with a well-defined, smooth, usually hornblende-rich rim. The modal mineralogy of the xenoliths is highly variable; they contain hornblende, plagioclase, phlogopite and orthopyroxene, with minor clinopyroxene, apatite, Fe–Ti oxides and rounded chromite. No olivine is observed. Small pockets of interstitial glass are present. The xenolith texture varies from poikilitic, with plagioclase oikocrysts in optical continuity, to granoblastic, indicating variable amounts of deformation and recrystallization. Small veins containing calcic plagioclase (e.g. An_{93}) and pyroxenes cut across some xenoliths. The xenoliths are interpreted as cumulates.

One of the samples (shiv01/#3) also contains a small (2–3 cm), elliptical, quench-textured andesitic enclave (Fig. 2a). There is no change in grain size towards the rim of the enclave, which is defined by the edges of crystals protruding into the host lava. The enclave has a high proportion of crystals (~85% calculated vesicle free) including randomly oriented, elongate, skeletal hornblende phenocrysts (Fig. 2a and b), phenocrysts of plagioclase, tabular Fe–Ti oxides, acicular apatite and, unusually, abundant anhydrite crystals up to 300 μm in length. Apatite is both more acicular, more abundant, and more S-rich than in the host andesite. Dendritic protrusions extend from the rims of some crystals (Fig. 2c, d). Mineral compositions are indistinguishable from compositions of phenocrysts in the host andesite (see Tables 3 and 4). The matrix comprises

Table 2: Temperatures estimated for the Shiveluch magma using different methods

T (°C)	Holland & Blundy (1994)		Andersen & Lindsley (1988); Stormer (1983) Ilm–mag	Putirka (2005) Plag–liquid	Total	Quenched enclave
	Hbl-hosted	Plag-hosted				
760	0	0	0	0	0	
780	0	2	0	0	2	
800	6	4	0	0	10	
820	12	4	0	1	17	2 (hb-plag)
840	6	2	1	11	20	1 (hb-plag)
860	18	5	7	22	52	
880	16	0	8	11	35	1 (ilm-mag)
900	11	0	13	7	31	1 (ilm-mag)
920	1	0	2	6	9	
940	0	0	1	1	2	
960	0	0	0	1	1	
980	0	0	1	3	4	
n	70	17	33	63	183	5
Average T	849	817	881	867		840
1σ	31·2	26·5	26·1	35·6		

''Hbl-hosted'' indicates inclusions of plagioclase in hornblende. ''Plag-hosted'' indicates inclusions of hornblende in plagioclase. Plag–liquid temperatures are calculated from melt inclusions and coexisting plagioclase host pairs. *n*, number of determinations.

a vesicle-rich, microlite-free, rhyolitic glass, with similar compositions to melt inclusions and matrix glasses in the host andesite. The enclave has slightly higher modal amphibole (Dirksen *et al.*, 2006, table 2) in comparison with the phenocryst assemblage in the host andesite, indicating a slightly more mafic bulk composition. Vesicles commonly occur between grain junctions, suggesting that vesiculation was induced by crystallization.

Whole-rock geochemistry

All samples studied here are pumices and dome rocks of medium-K andesite (Gill, 1981), and plot in the calc-alkaline field of Miyashiro (1974). The rocks contain 61–63 wt % SiO_2. Figure 3 shows selected major and trace element variation diagrams for whole-rock data from these samples (see also Dirksen *et al.*, 2006, table 1). Negative correlations with SiO_2 are seen in MgO, CaO and FeO. Al_2O_3 and K_2O do not vary much; Na_2O correlates positively with SiO_2 (Fig. 3). In the trace elements, weak positive trends with SiO_2 are seen for Ba, Rb, Sr and Zr; Y shows little variation; V defines negative trends. Typical compositions of hornblende and plagioclase phenocrysts from electron probe microanalysis (EPMA) and secondary ion mass spectrometry (SIMS) data are also plotted in Fig. 3. Most major element trends are broadly consistent with fractionation of an assemblage dominated by plagioclase and hornblende. However, the trace element trends suggest the involvement of an additional phase, in which Ba, Rb and V, as well as K_2O, are compatible (Fig. 3). Phlogopite, along with titanomagnetite, is a suitable candidate (Fig. 3). Phlogopite is found with hornblende and plagioclase in cumulate xenoliths, and occasionally as inclusions in phenocrysts.

ANALYTICAL METHODS

Wavelength-dispersive EPMA of minerals and glasses was performed at the University of Bristol using a CAMECA SX-100 five-spectrometer instrument. Minerals were analysed using a 20 kV accelerating voltage, 10 nA beam current and a 5 μm beam diameter. Groundmass glasses and melt inclusions were analysed using a 15 kV accelerating voltage, 2–4 nA beam current and a 15 μm beam diameter, with Na and Si analysed first to reduce the effects of alkali migration, as described in Humphreys *et al.* (2006). Data reduction was performed online using a stoichiometric PAP correction model (Pouchou & Pichoir, 1984). H_2O contents of hydrous melt inclusions, and adjacent host plagioclase compositions, were estimated as described by Blundy *et al.* (2006), and were presented in that study.

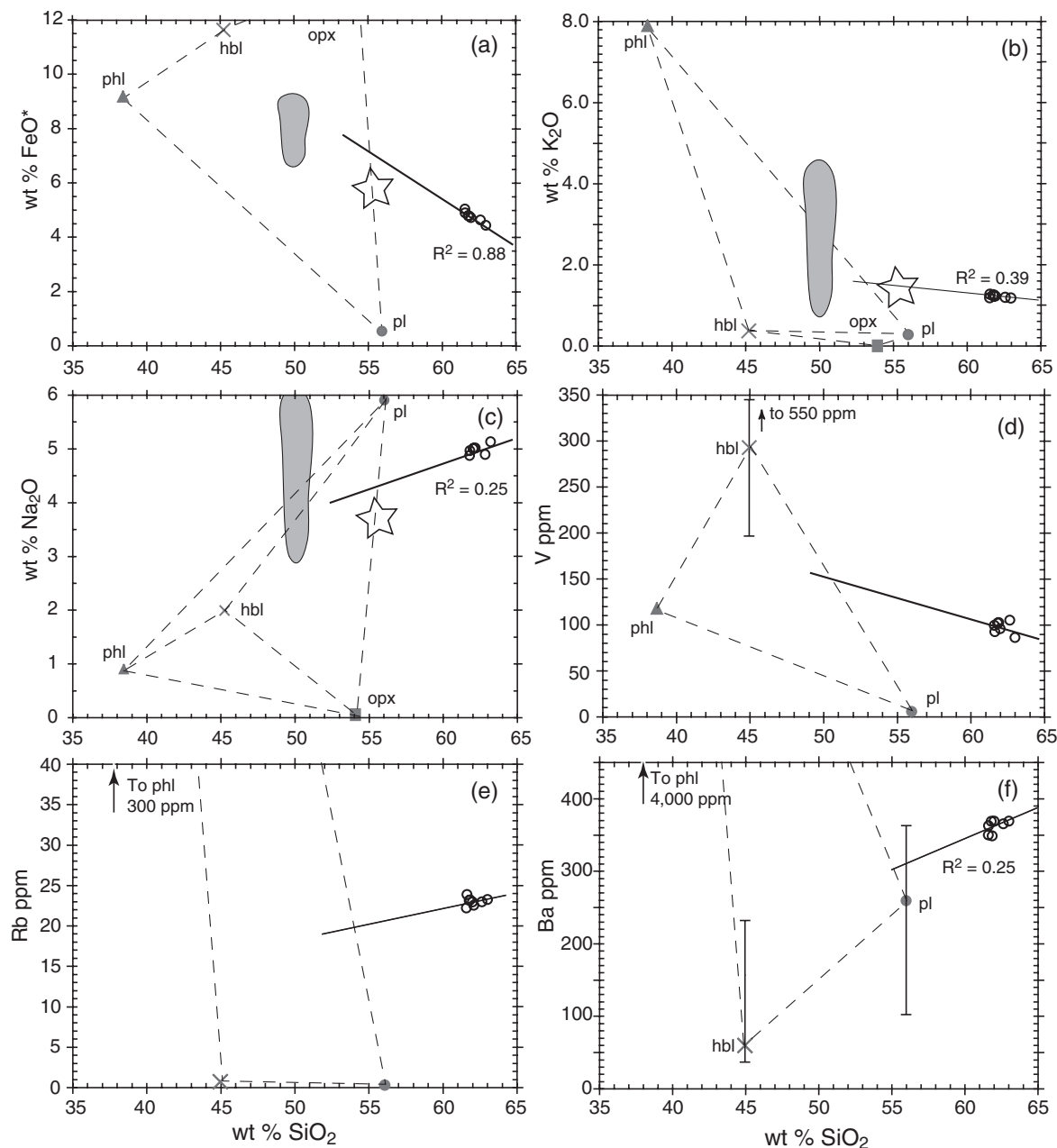X-ray fluorescence (XRF) analyses were carried out using a Philips PW1400 X-ray fluoresence spectrometer

Fig. 3. Anhydrous, whole-rock major element (a–c) and trace element (d–f) variation diagrams for the samples studied. Typical hornblende (hbl) and plagioclase (plag) compositions are plotted from EPMA or SIMS analyses, with error bars indicating the range of LA-ICP-MS data where available. Phlogopite compositions are taken from Tischendorf *et al.* (2001). Trend lines with R^2 quoted represent least-squares regression lines; other trend lines are fitted by eye. Grey shaded areas indicate approximate whole-rock compositions of cumulate nodules, reconstructed from modal data (Humphreys, 2006). Star indicates the approximate composition of the quenched enclave, also reconstructed from modal data.

at Leicester University. Analyses of major elements were performed using fused glass discs made from powders mixed with 80:20 Li metaborate:Li tetraborate. Trace elements were determined on 32 mm diameter, pressed powder briquettes.

Trace element concentrations in some hornblende and plagioclase phenocrysts were determined by inductively coupled plasma mass spectrometry (ICP-MS) using a VG Elemental PlasmaQuad 3 system coupled to a VG LaserProbe II (266 nm frequency-quadrupled Nd–YAG laser) at the University of Bristol. He gas was the ablation medium and a He–Ar mixture carried the sample to the plasma. The laser beam was set to 20 μm diameter, 5 Hz repetition rate and about

25–30 J/cm^2 energy density. For each analysis, counts were collected on the background for 50 s, before firing the laser and collecting counts for 50 s. Data were collected for ^{45}Sc, ^{51}V, ^{88}Sr, ^{90}Zr and ^{130}Ba. The glass NIST 610 (Pearce *et al.*, 1997) was used as primary standard, with NIST 612 as a secondary standard. Data reduction, using the method of Longerich *et al.* (1996) and Si as the internal standard, was performed using PlasmaLab software.

ESTIMATION OF INTENSIVE PARAMETERS

Temperature

Magma temperatures for the Shiveluch andesite were estimated by Dirksen *et al.* (2006) using methods including hornblende–plagioclase thermometry and Fe–Ti oxide thermometry. Here, we summarize these temperature estimates and present further information derived from plagioclase–liquid equilibria (Putirka, 2005), which constrains T from information about X_{An} in plagioclase, liquid composition (from melt inclusions), H_2O content, and pressure, assuming equilibrium between plagioclase and the coexisting liquid. Pressure was calculated from H_2O content using the model of Newman & Lowenstern (2002). This approach is valid because there is good evidence that the magma is H_2O-saturated (see later). Results are given in Table 2.

Hbl–plag temperatures range from 775°C to 906°C ± 35°C, with an average of 841°C ± 35°C ($n = 85$). A temperature of 808–836°C ± 35°C was obtained for the quenched enclave ($n = 3$). In comparison, Fe–Ti oxide temperatures range from 834°C to 978°C (Table 2), with an average of 878°C ($n = 32$). Microlites in contact with the matrix glass return slightly higher temperatures (860–978°C) than inclusions in phenocrysts (834–904°C). An oxide–oxide temperature of ~870°C was estimated for the andesite enclave ($n = 2$). Plagioclase–liquid temperatures range from 819°C to 975°C, with an average of 867°C ($n = 63$). These data cover a wide range of temperatures; oxide and plagioclase–liquid temperatures are consistently higher than hbl–plag temperatures. These differences are interpreted to reflect temperature variations throughout the magma's evolution. Hbl–plag data reflect temperatures early in the magmatic history, while hornblende is still crystallizing. Oxide data, which re-equilibrate rapidly (Hammond & Taylor, 1982; Venezky & Rutherford, 1999), are interpreted to reflect higher magma temperatures caused by release of latent heat during late-stage decompression-driven crystallization (Blundy *et al.*, 2006). Plagioclase–liquid temperatures reflect real variation of T and pH_2O during the magma's history. From these data, we estimate that magma temperatures prior to ascent were ~840°C.

Pressure

The maximum magma pressure, estimated from the maximum H_2O contents of melt inclusions, is ~160 MPa (Humphreys, 2006). The depth of the magma chamber roof at Shiveluch Volcano is thus assumed to be ~5–6 km below the summit, a result consistent with seismic data (Dirksen *et al.*, 2006).

Oxygen fugacity

Oxygen fugacity is estimated from Fe–Ti oxide equilibria using the method of Andersen *et al.* (1993). Values of $\log(fO_2)$ obtained are highly oxidizing, and range from –9·0 to –11·2, with an average of –10·3 (Fig. 4). The values obtained correspond to 1·5–2·1 log units above the nickel–nickel oxide (NNO) buffer [quartz–fayalite–magnetite (QFM) + 2·1 to + 2·7], with an average of NNO + 1·9. The andesite enclave gave NNO + 1·8. Uncertainties are approximately ±0·6 log units (Andersen *et al.*, 1993). These oxidizing conditions are consistent with the co-precipitation of sulphides (S^{2-} oxidation state) with anhydrite (S^{6+}) and S-bearing apatite (S^{6+}) (Carroll & Rutherford, 1985, 1988).

PHENOCRYST ZONING PATTERNS

Plagioclase

Three plagioclase phenocryst textures are observed: oscillatory zoning, patchy zoning and sieve texture. Table 3 gives representative compositions of the phenocryst types, and Fig. 5 summarizes the chemical variations between the textures.

Oscillatory zoned phenocrysts (~68–75% of plagioclase) typically have rather diffuse, symmetrical zones in their cores, in contrast to the sharper, more asymmetrical boundaries of outer zones (Fig. 6a and b). This may reflect partial re-equilibration of the cores during long residence times in the magma chamber. Compositional variation in oscillatory zoning is typically less than 30 mol % Anorthite. Inner zones show an approximately inverse relationship between Fe/Al and X_{An}. Outer zones commonly show a sharp boundary to higher X_{An}, followed by gradual decay to more sodic compositions (Fig. 6a and b). At some outer zone boundaries resorption has taken place, as shown by irregular surfaces (Fig. 7a and b) and rounded corners (Fig. 7c). Melt inclusions are occasionally trapped at these resorption boundaries. Rim compositions are usually consistent across each sample. The rims of oscillatory zoned crystals typically show a gradual increase in the
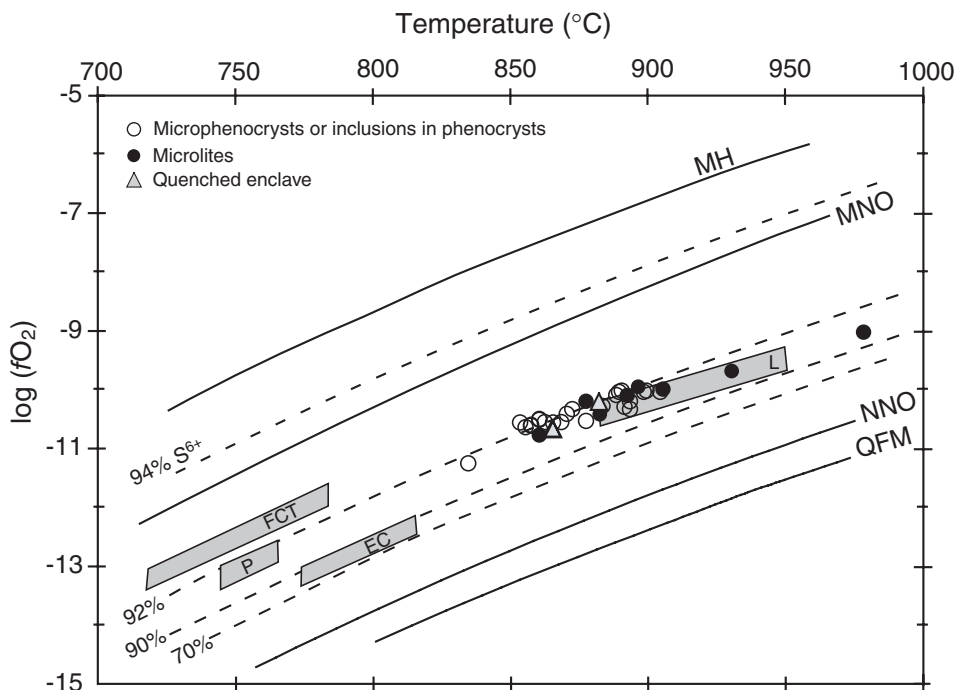
Fig. 4. Temperature vs oxygen fugacity, estimated from Fe–Ti oxide equilibria in Shiveluch samples using the QUILF program (Andersen *et al.*, 1993). Oxides were recalculated using Stormer (1983). Contours represent percent of sulphur existing as oxidized sulphate (S^{6+}), calculated from Carroll & Rutherford (1988). QFM, NNO, MNO and MH buffers are plotted for comparison. Shaded areas represent other silicic, sulphur-rich magmas: Pinatubo (P), Lascar (L), El Chichòn (EC) and the Fish Canyon Tuff (FCT). MNO=manganese oxide; MH=magnetite-haematite.

ratio Fe/Al over several zones (Fig. 6), unaccompanied by changes in Mg. Groundmass plagioclase also has higher Fe contents and Fe/Al values (Fig. 5b), as observed in other orogenic andesites (e.g. Nakada & Motomura, 1999; Murphy *et al.*, 2000). Fe in plagioclase is dominated by Fe^{3+} at high fO_2 (Sugawara, 2000), and is therefore mainly incorporated by substituting for Al^{3+} (Longhi *et al.*, 1976; Sugawara, 2000). Fe^{3+} increases with X_{An} because the number of available Al^{3+} sites increases (Hofmeister & Rossman, 1984). Thus the ratio Fe/Al provides a measure of the proportion of Al sites occupied by Fe.

Patchy zoned crystals (~20–25% of plagioclase) have an irregular or chequerboard, central corroded core with abundant melt and mineral inclusions, suggesting partial resorption of an older core. In back-scattered scanning electron microscope (SEM) images, melt inclusions are closely associated with more albitic (darker) plagioclase of $An_{29–54}$ (Fig. 8a). This suggests that the more An-rich patches ($An_{42–74}$, Fig. 8a) formed the original core, and that the more albitic plagioclase crystallized after partial resorption, causing entrapment of melt inclusions. The change in X_{An} between early, anorthite-rich (brighter) plagioclase and later, albite-rich (darker) plagioclase is typically not accompanied by changes in minor elements (e.g. Fe, Mg). Trace element contents do

vary, however: An-rich patches typically contain 120–220 ppm Ba whereas Ab-rich patches contain 210–360 ppm Ba. Sr contents are similar (920–1520 ppm Sr in An-rich patches, 1000–1400 ppm in Ab-rich patches). The rims of patchy phenocrysts ($An_{37–57}$) are typically clear and zoned; many show oscillatory zoning (Figs 6c and 7d). In the oscillatory zoned rims, the same range of X_{An} and pattern of increasing Fe/Al is observed as in oscillatory phenocrysts (Fig. 6c). Outermost individual zones can be correlated between the two phenocryst types (Fig. 6), implying that they had a common magmatic history during the late stages of crystallization.

Sieve-textured phenocrysts (~3–9% of plagioclase) have a sodic core ($An_{34–37}$, Fig. 5a), surrounded by a narrow rim of more An-rich plagioclase (Fig. 5b). The core is commonly anhedral, and in some crystals oscillatory zonation is observed in the core (Fig. 9a). The boundary between the core and rim comprises a network of micrometre-scale melt channels. The channelized zone is usually a narrow ring (Fig. 9b), but sometimes occupies the whole plagioclase interior (Fig. 9c); these variations could be an artefact of sectioning, or related to the extent of disequilibrium encountered by the crystal (Clynne, 1999). Where hornblende inclusions are present in both core and rim of sieved phenocrysts (Fig. 9d), temperatures estimated

Table 3: *Representative compositions and structural formulae of patchy, sieve, oscillatory and other plagioclase phenocrysts and microlites*

Patchy plagioclase

Grain:	shv2-29			shv2-12			shv3-2		
Position:	Bright	Dark	Rim	Bright	Dark	Rim	Bright	Dark	Rim
SiO_2	51·65	54·35	58·15	50·88	56·56	53·55	50·92	57·20	57·26
Al_2O_3	30·34	28·67	26·07	30·63	27·05	29·10	30·73	27·08	26·38
FeO*	0·40	0·31	0·37	0·35	0·29	0·35	0·36	0·31	0·37
MgO	0·01	0·01	0·02	0·00	0·01	0·01	0·00	0·02	0·01
CaO	13·30	11·33	8·20	13·86	9·42	11·89	13·87	9·14	8·61
Na_2O	4·07	5·32	6·70	3·88	6·23	4·95	3·72	6·29	6·57
K_2O	0·10	0·16	0·26	0·10	0·22	0·13	0·11	0·25	0·23
Total	99·86	100·14	99·77	99·70	99·78	99·98	99·71	100·29	99·43
Si	2·372	2·480	2·643	2·344	2·579	2·450	2·344	2·591	2·616
Al	1·642	1·541	1·396	1·663	1·453	1·569	1·667	1·446	1·420
Fe	0·015	0·012	0·014	0·013	0·011	0·013	0·014	0·012	0·014
Mg	0·001	0·001	0·001	0·000	0·001	0·001	0·000	0·001	0·001
Ca	0·654	0·554	0·399	0·684	0·460	0·583	0·684	0·444	0·421
Na	0·362	0·471	0·590	0·347	0·551	0·439	0·332	0·552	0·582
K	0·006	0·009	0·015	0·006	0·013	0·008	0·006	0·014	0·013
Total	5·046	5·058	5·044	5·052	5·054	5·055	5·041	5·046	5·054
X_{An}	0·64	0·54	0·40	0·66	0·45	0·57	0·67	0·44	0·41
X_{Or}	0·01	0·01	0·01	0·01	0·01	0·01	0·01	0·01	0·01
Fe/Al	0·009	0·007	0·009	0·008	0·008	0·008	0·008	0·008	0·010

Sieve plagioclase

Grain:	shiv012-16		shiv012-17		shiv013-24		shv3-51		shiv013-18	
Position:	Core	Rim	Core	Rim	Core	Rim	Core	Rim	Core	Rim
SiO_2	58·84	54·94	58·69	55·22	58·83	55·49	58·57	54·53	60·17	53·90
Al_2O_3	25·93	28·47	25·81	28·22	25·24	27·61	25·92	28·21	25·13	28·42
FeO*	0·13	0·45	0·18	0·46	0·21	0·37	0·16	0·44	0·35	0·43
MgO	0·00	0·03	0·00	0·03	0·00	0·02	0·00	0·03	0·01	0·03
CaO	7·51	10·94	7·63	10·77	7·42	9·92	7·69	10·81	7·07	10·86
Na_2O	0·27	0·13	0·22	0·12	7·34	5·94	7·33	5·68	7·45	5·71
K_2O	6·85	5·20	6·93	5·32	0·41	0·16	0·21	0·11	0·39	0·11
Total	99·53	100·16	99·46	100·14	99·44	99·51	99·88	99·81	100·57	99·46
Si	2·637	2·477	2·635	2·488	2·682	2·541	2·659	2·498	2·708	2·481
Al	1·370	1·512	1·366	1·499	1·356	1·490	1·387	1·523	1·333	1·541
Fe	0·005	0·017	0·007	0·017	0·008	0·014	0·006	0·017	0·013	0·016
Mg	0·000	0·002	0·000	0·002	0·000	0·001	0·000	0·002	0·001	0·002
Ca	0·361	0·528	0·367	0·520	0·362	0·487	0·374	0·531	0·341	0·536
Na	0·023	0·011	0·019	0·010	0·648	0·527	0·645	0·505	0·650	0·509
K	0·392	0·299	0·397	0·306	0·024	0·009	0·012	0·006	0·023	0·007
Total	4·396	4·548	4·393	4·537	5·057	5·061	5·071	5·075	5·045	5·085
X_{An}	0·46	0·63	0·47	0·62	0·35	0·48	0·36	0·51	0·34	0·51
X_{Or}	0·50	0·36	0·51	0·37	0·02	0·01	0·01	0·01	0·02	0·01
Fe/Al	0·003	0·011	0·004	0·011	0·005	0·009	0·004	0·011	0·010	0·010

Table 3: continued

Grain:	Oscillatory plagioclase								
	shiv012-8			m12s25			shiv013-24		
Position:	Core	Intermed	Rim	Core	Intermed	Rim	Core	Intermed	Rim
SiO_2	58·4	54·12	57·1	58·18	59·84	56·95	54·14	56·28	56·74
Al_2O_3	25·83	28·65	26·61	26·62	25·47	26·49	28·2	27·41	27·23
FeO*	0·31	0·32	0·35	0·29	0·29	0·46	0·32	0·31	0·33
MgO	0·01	0·00	0·01	0·00					
CaO	0·79	11·16	8·89	8·63	7·37	9·02	11·06	9·74	9·24
Na_2O	6·66	5·10	6·2	6·33	6·87	6·05	5·4	6·11	6·34
K_2O	0·27	0·15	0·24	0·24	0·31	0·17	0·19	0·24	0·19
Total	92·27	99·50	99·40	100·29	100·15	99·14	99·31	100·09	100·07
Si	2·779	2·481	2·606	2·627	2·697	2·606	2·491	2·561	2·579
Al	1·449	1·548	1·431	1·417	1·353	1·429	1·529	1·470	1·458
Fe	0·012	0·012	0·013	0·011	0·011	0·018	0·012	0·012	0·013
Mg	0·001	0·000	0·001	0·000	0·000	0·000	0·000	0·000	0·000
Ca	0·040	0·548	0·435	0·417	0·356	0·442	0·545	0·475	0·450
Na	0·615	0·453	0·549	0·554	0·600	0·537	0·482	0·539	0·559
K	0·016	0·009	0·014	0·014	0·018	0·010	0·011	0·014	0·011
Total	4·896	5·043	5·035	5·026	5·016	5·032	5·059	5·056	5·058
X_{An}	0·06	0·54	0·44	0·42	0·37	0·45	0·53	0·46	0·44
X_{Or}	0·02	0·01	0·01	0·01	0·02	0·01	0·01	0·01	0·01
Fe/Al	0·008	0·008	0·009	0·007	0·007	0·012	0·008	0·007	0·008

Grain:	Groundmass plagioclase						Quenched enclave plagioclase			
	shv2-23	shv2-6	shv3-5	shv3-20	shv3-23	shv3-25	shiv013-21	shiv013-37	shiv013-27	shiv013-7
Position:										
SiO_2	55·24	55·97	56·90	55·88	55·79	55·66	58·43	57·29	57·46	57·71
Al_2O_3	27·82	27·24	26·65	27·32	28·09	27·29	25·46	26·52	26·68	26·32
FeO*	0·68	0·57	0·52	0·53	0·58	0·49	0·38	0·43	0·38	0·37
MgO	0·07	0·06	0·05	0·03	0·05	0·05	0·02	0·02	0·02	0·02
CaO	10·54	9·91	9·24	10·02	10·62	10·04	7·64	8·67	8·97	8·52
Na_2O	5·72	5·91	6·32	5·87	5·53	5·81	7·28	6·65	6·53	6·64
K_2O	0·11	0·14	0·17	0·14	0·12	0·13	0·28	0·24	0·22	0·24
Total	100·22	99·83	99·88	99·82	100·83	99·51	99·53	99·85	100·27	99·85
Si	2·520	2·556	2·594	2·552	2·524	2·550	2·666	2·610	2·606	2·625
Al	1·495	1·466	1·432	1·471	1·498	1·473	1·369	1·424	1·426	1·411
Fe	0·026	0·022	0·020	0·020	0·022	0·019	0·014	0·016	0·014	0·014
Mg	0·005	0·004	0·003	0·002	0·003	0·003	0·001	0·001	0·001	0·001
Ca	0·515	0·485	0·451	0·490	0·515	0·493	0·374	0·423	0·436	0·415
Na	0·506	0·523	0·558	0·519	0·485	0·516	0·644	0·588	0·574	0·585
K	0·007	0·008	0·010	0·008	0·007	0·008	0·016	0·014	0·013	0·014
Total	5·067	5·055	5·058	5·055	5·047	5·054	5·069	5·062	5·057	5·052
X_{An}	0·50	0·48	0·44	0·48	0·51	0·48	0·36	0·41	0·43	0·41
X_{Or}	0·01	0·01	0·01	0·01	0·01	0·01	0·02	0·01	0·01	0·01
Fe/Al	0·017	0·014	0·013	0·014	0·014	0·012	0·010	0·011	0·010	0·010

Typical 1 S.D. are: SiO_2 ±0·15; Al_2O_3 ±0·1; FeO* ±0·02; MgO ±0·01; CaO ±0·08; Na_2O ±0·05; K_2O ±0·01.
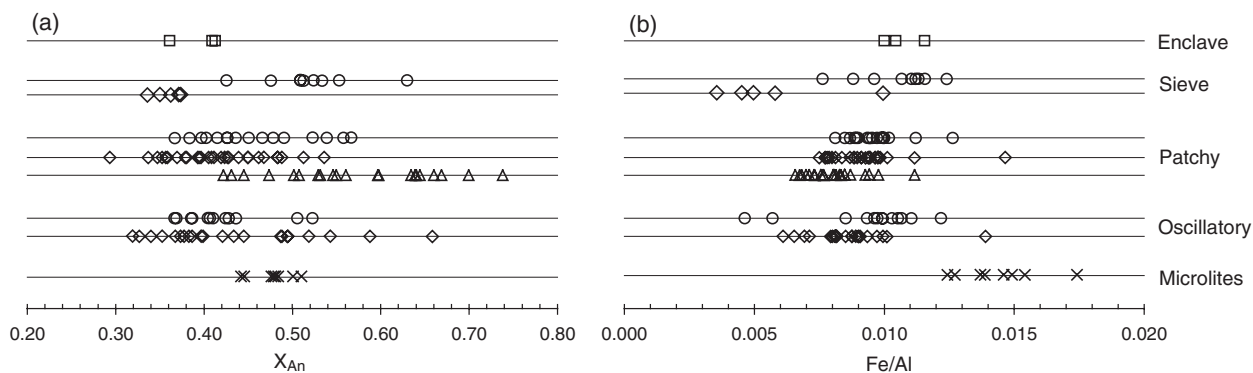
Fig. 5. X_{An} and Fe/Al compositions of the plagioclase textural types. Circles indicate rim compositions; core compositions are represented by diamonds, or by diamonds (dark patches) and triangles (bright patches) for patchy plagioclase.

using hbl–plag geothermometry suggest an increase of about 50°C from the core to the rim. Rims of sieved plagioclase crystals have higher FeO (e.g. 0·43 wt % compared with 0·21 wt %), Fe/Al (e.g. 0·010 compared with 0·005), MgO (0·03 wt % compared with 0·00 wt %) and X_{An} (An_{43-63} compared with An_{34-37}) than the cores (Table 3). Concentrations of Ba and Sr are very similar in both cores and rims of the sieve plagioclase. These cores are sodic compared with typical oscillatory plagioclase compositions, but similar to the Ab-rich patchy plagioclase (Fig. 5a; Table 3).

Hornblende

Many hornblende phenocrysts (65–80%) are compositionally rather uniform, unzoned magnesio-hornblendes. However, the compositions of unzoned hornblendes vary in terms of Al^{iv}, Al^{vi}, Mg-number and $(Na,K)^A$ (Fig. 10). Three other textural types are observed: patchy zoning (<10% of phenocrysts), simple zoning (4–20%) and multiple zoning (0–3%) (Fig. 11; Table 4). Overall, hornblendes show a very weak Al^{iv}–Al^{vi} (Tschermak) correlation ($R^2 = 0·30$; $n = 420$) (Fig. 12a). No correlation is observed within any single zoned phenocryst (Fig. 12b), but multiple analyses from the same grain plot in a cluster around a given Al^{iv}–Al^{vi}. Rims of patchy zoned crystals have lower Al^{iv}–Al^{vi} than simple-zoned phenocrysts (Figs 10 and 12b). Qualitatively, this relationship indicates rim crystallization at lower pressure, though quantitative estimates cannot be made because of the lack of K-fsp and quartz in the crystallizing assemblage (Johnson & Rutherford, 1989). Overall there is a good correlation ($R^2 = 0·69$) between Al^{iv} and $(Na,K)^A$ (Fig. 12c), indicating that hornblende crystallization is controlled by the edenite exchange. Multiple analyses from single zoned phenocrysts commonly show a good correlation (e.g. $R^2 = 0·9$ or better, Fig. 12d) and can span a wide range of Al^{iv} and $(Na,K)^A$ (Fig. 10a and d).

Patchy zoning in hornblende phenocryst cores (Fig. 11a) comprises irregularly shaped dark and light patches in back-scattered SEM images (Fig. 8b). The crystals often contain abundant mineral and melt inclusions. The texture is strongly reminiscent of patchy zoning in plagioclase (see Fig. 8a). Melt inclusions are commonly associated with brighter patches (Fig. 8b), and mineral inclusions are commonly edged with a sliver of melt, suggesting that they grew from a pre-existing melt pool. Bright regions have higher Al^{iv} and $(Na,K)^A$, and lower Mg-number than dark regions (Fig. 10; Table 4). Bright and dark regions are indistinguishable in terms of trace elements, except for Ba, which is slightly more abundant in the Al-rich hornblende (Fig. 13a). This probably results from the higher A-site occupancy of the Al-rich hornblende (Table 4), with Ba substituting for K (Tiepolo et al., 2003). Patchy phenocrysts are sometimes overgrown by a thin, euhedral, oscillatory-zoned rim (Fig. 14a–c), with a good correlation of Al^{iv} with $(Na,K)^A$ (Fig. 14c). Each new zone is marked by a small but abrupt increase in Mg-number, and decrease in Al^{iv} and $(Na,K)^A$ (Fig. 14a). Throughout the remainder of each zone the Mg-number, and Al^{iv} and $(Na,K)^A$ contents return to near original levels (Fig. 14a).

Simple-zoned hornblende phenocrysts are characterized by a fairly uniform core, and a sharp change in composition to the rim (Figs 11b and 14d–f), with only occasional evidence of embayment or rounding. Al^{iv} and $(Na,K)^A$ are well correlated (Fig. 14f). Rims have higher Mg-number (Fig. 14e), Na and Si, higher Fe^{3+}/Fe^{2+} (calculated using Holland & Blundy, 1994), and lower Ti and Fe compared with the cores (i.e. reverse zoning, Table 4; Fig. 10). Within a single phenocryst core, Al^{iv} and $(Na,K)^A$ may show a slight rimward decrease, with a corresponding increase in Mg-number (Fig. 14d). Cores and rims are indistinguishable in terms of trace elements. Normally zoned phenocrysts, with cores similar in composition to the rims of reverse simple zoned crystals, are rare.
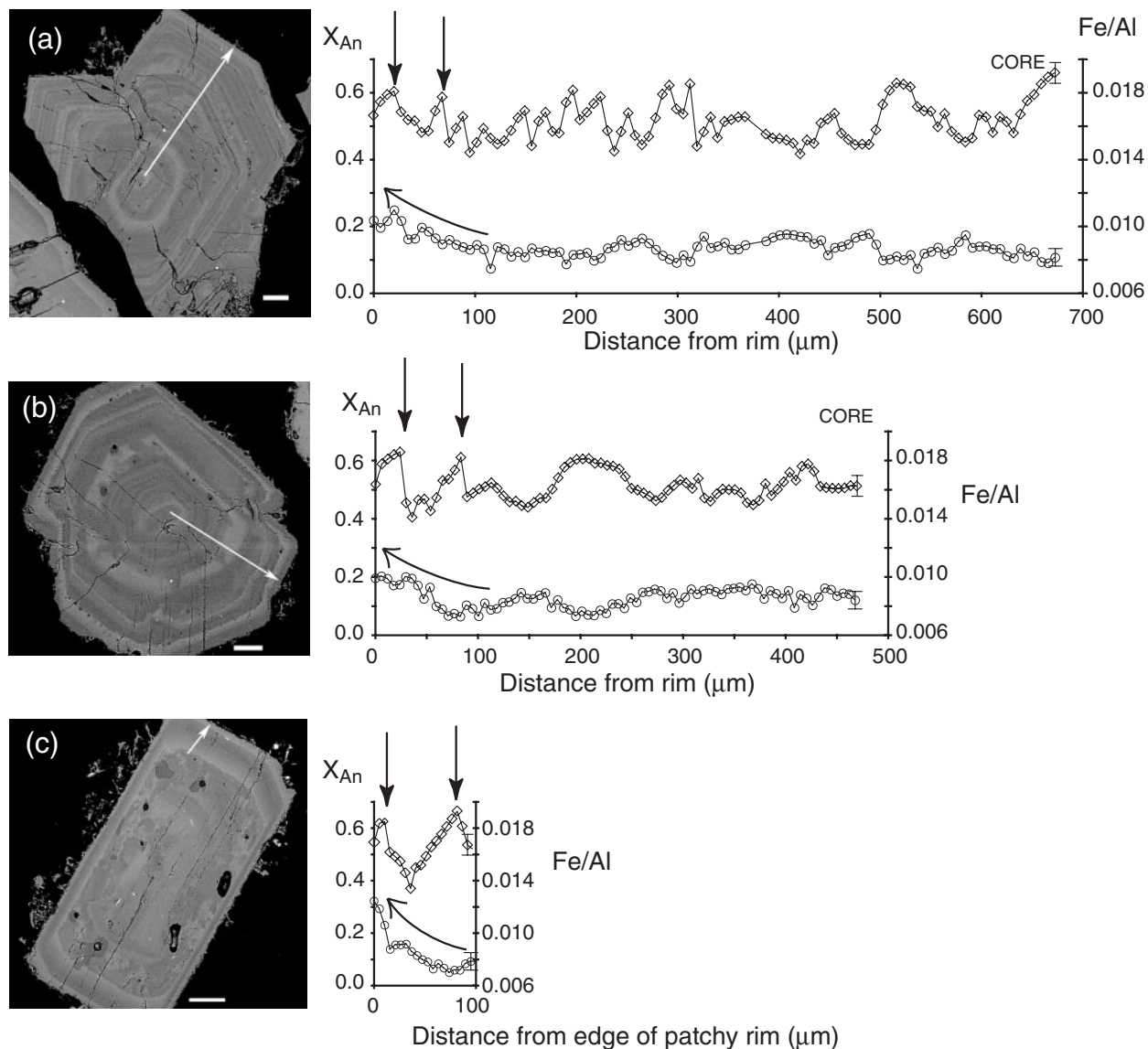
Fig. 6. Typical zoning profiles of X_{An} (diamonds) and Fe/Al (circles) from oscillatory zoned phenocrysts (a, b) and rims of patchy phenocrysts (c). All crystals come from the same sample. White arrows mark the line of each traverse. X_{An} zoning is characterized by sharp increases in An content, followed by slower decay. Zones are typically more diffuse near the core of the crystal than at the rim. Some zoning patterns near the rims (downward arrows) can be tentatively matched across different phenocrysts. Scale bar represents 100 μm. Crystals also show a gradual, rimward increase in Fe/Al (curved arrows). Error bars represent typical 1 S.D. for X_{An} and Fe/Al, calculated from EPMA counting statistics.

Zonation in multiple-zoned hornblendes (Fig. 14g–i) is texturally similar to that in simple-zoned hornblendes, but the zones are less clearly defined (Fig. 11c). Zoning is characterized by broad, diffuse zones that lack correlation of Al^{iv} with Mg-number (Fig. 14h) or $(Na,K)^A$ (Fig. 14i), and are marked by large jumps in Mg-number (Fig. 14g); for example, from ∼77 to ∼58 and back. Dark zones have high Mg-number, Na and Si, and low Ti, Mn, K and Fe compared with bright zones (Fig. 10).

Apatite

Both normal and reverse zoning patterns are observed in apatite. Normally zoned crystals have a rimward increase in S, whereas reversely zoned crystals have a rimward decrease. S correlates with Na_2O (Fig. 15), suggesting a coupled substitution mechanism such as $S^{6+} + Na^+ = P^{5+} + Ca^{2+}$ (Liu & Comodi, 1993) or $2S^{6+} + 4REE^{3+} + Si^{4+} + 2Na^+ = 4P^{5+} + 5Ca^{2+}$ (Parat *et al.*, 2002). In general, microphenocrysts and microlites from the quenched enclave are more sulphur-rich
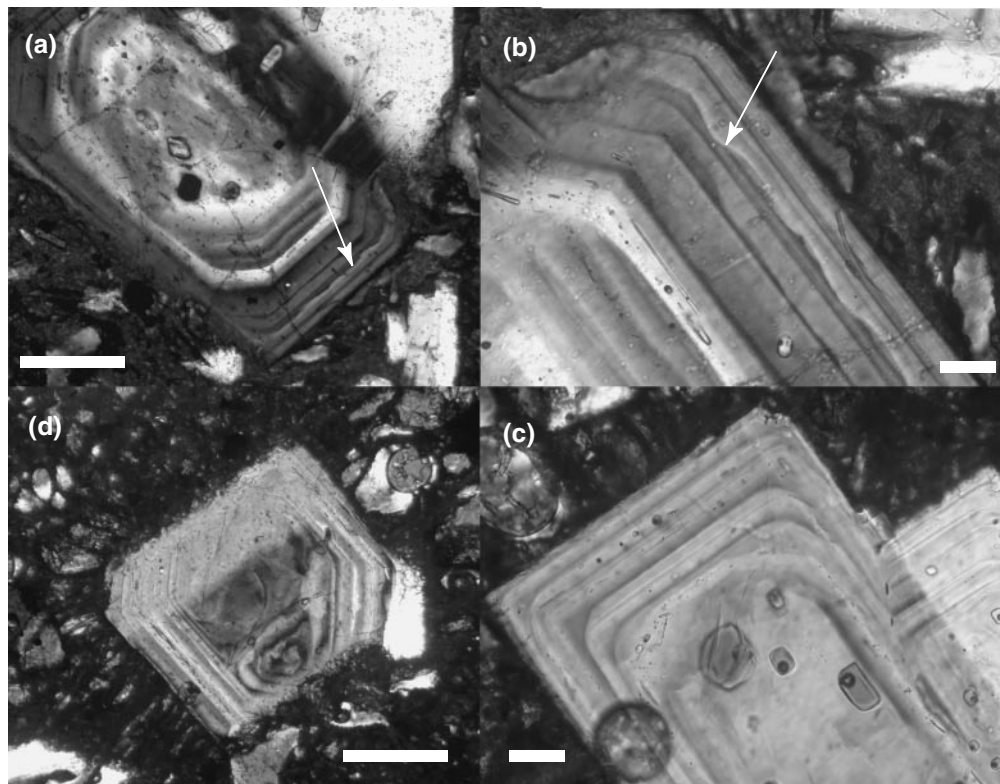
Fig. 7. Petrographic features of patchy and oscillatory zoned plagioclase. Resorption occurs at some boundaries leaving irregular, wavy zoning surfaces (a, b) and rounded corners (c). Some patchy zoned plagioclase have a well-developed oscillatory-zoned rim (d). Scale bars represent 200 μm (a, d) and 50 μm (b, c).

(550–5860 ppm) than those from the host andesite (235–3300 ppm, Fig. 15).

Olivine

Olivine occurs as large, isolated crystals of composition Fo_{80-87}, and occasionally contains inclusions of En-rich orthopyroxene and chromite. Strong evidence of disequilibrium is seen, varying from a reaction corona of titanomagnetite, orthopyroxene and amphibole, to complete replacement by sub-grains of ortho-pyroxene, titanomagnetite, amphibole and sometimes plagioclase. The remnant olivine is commonly strongly zoned, with Mg decreasing rimward. These reaction rims are attributed to reaction of olivine with a silica-rich, oxidizing melt (e.g. van Lamoen, 1979; Arculus & Wills, 1980; Matthews et al., 1994; Dirksen et al., 2006).

DISCUSSION

Crystal zoning and dissolution textures are produced by changes in some combination of pressure (P), tempera-ture (T), pH_2O, fO_2 or melt composition. Changes in these parameters reflect physical processes acting at different stages of the magmatic history. For example, prolonged periods of cooling and fractional crystal-lization in the deep crust result in the segregation of evolved, H_2O-rich residual melts (Annen et al., 2006). Magmas ascending from depth may bring with them old crystals or cumulates (e.g. Turner et al., 2003), which may become resorbed during ascent (Dungan & Davidson, 2004). Once stored in a shallow magma chamber, the magma may experience continued crystal fractionation, cooling, convection, mixing or mingling with new magmas of the same or different compositions, oxidation–reduction processes, decompression during magma ascent and pressure fluctuations related to eruptive processes. In this section we attempt to ascribe individual phenocryst textures to specific events or processes in the magmatic history. Figure 16 summarizes the textural features and geochemical characteristics of each type of zoning discussed.

Origin of patchy zoning
Patchy zoning in plagioclase

Patchy plagioclase is characterized by an irregular, partially resorbed, An-rich, Ba-poor core, filled in and overgrown by Ab-rich, Ba-rich plagioclase that trapped
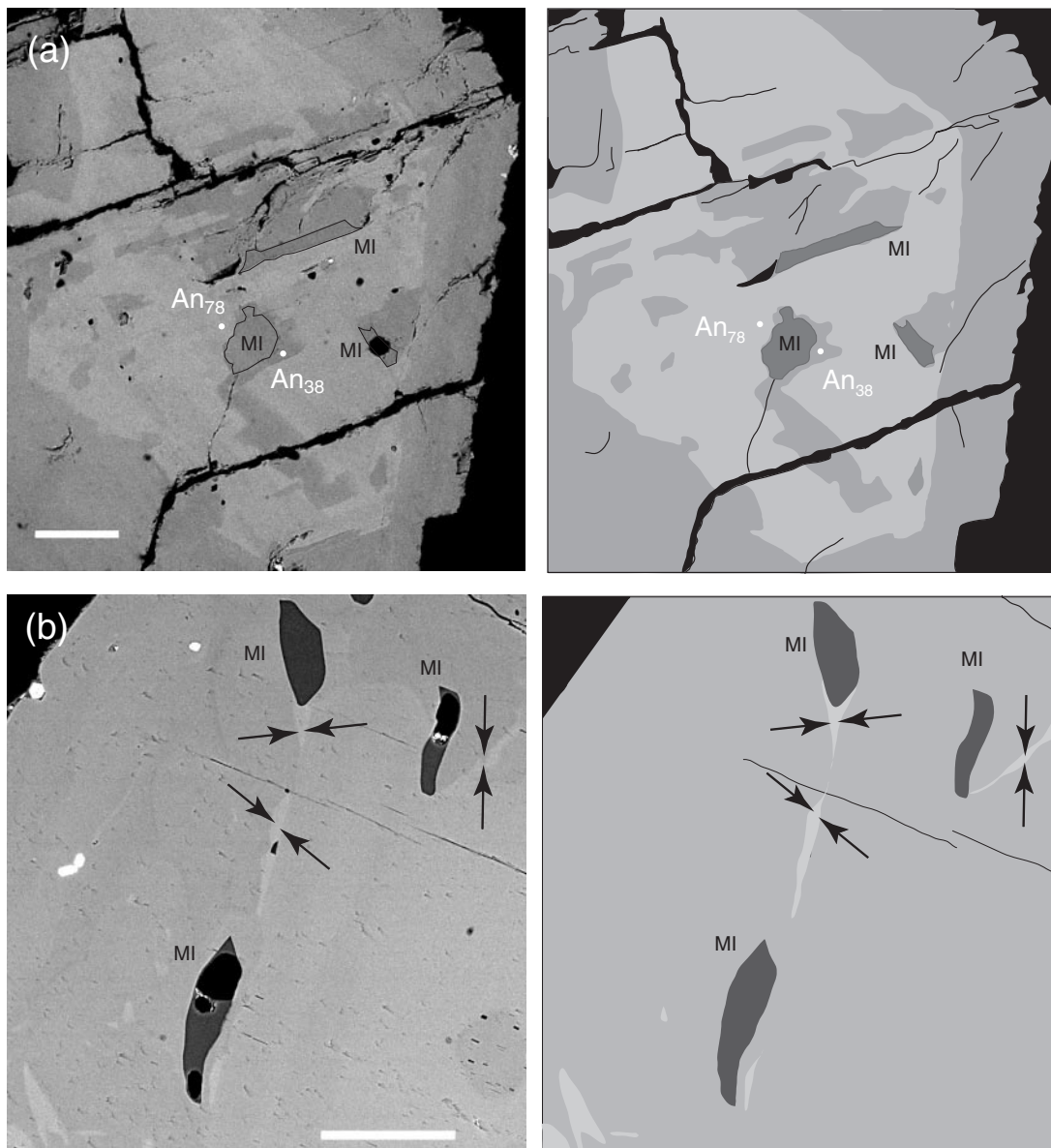
Fig. 8. (a) Left: backscattered SEM photograph showing typical patchy texture in plagioclase; right: line sketch highlighting the main features. Melt inclusions (dark grey) are closely associated with the darker, albitic plagioclase. This indicates that the Ab-rich surrounding plagioclase formed, and melt inclusions were trapped, after partial resorption of the original, An-rich core. White circles indicate positions of analyses. (b) Left: backscattered SEM photograph; right: sketch showing typical patchy texture in hornblende. Melt inclusions (MI, dark grey) are associated with stringers of more Al-rich (brighter) hornblende (pairs of black arrows). This implies that the brighter hornblende crystallized from melt, concurrent with entrapment of melt inclusions, after partial dissolution of the more Al-poor (darker) core. Scale bars represent 100 μm.

abundant melt inclusions (Fig. 16a). Similar textures have previously been attributed to skeletal growth (e.g. Kawamoto, 1992) or partial dissolution (e.g. Vance, 1965; Gerlach & Grove, 1982). Here, we suggest that the patchy texture forms as a result of partial resorption during magma ascent.

Under equilibrium conditions, the concentrations of minor and trace elements in plagioclase are controlled by melt concentrations and partition coefficients

(Ginibre *et al.*, 2002). We calculated Ba and Sr concentrations of melts coexisting with patchy plagioclase using the method of Blundy & Wood (1991) for $T = 840°C$. In general, the calculations indicate that early, An-rich plagioclase was in equilibrium with melts considerably enriched in Ba and Sr compared with the Ab-rich plagioclase (Fig. 17a). The concentrations of Ba and Sr in the melt in equilibrium with early, An-rich plagioclase decrease markedly from approximately
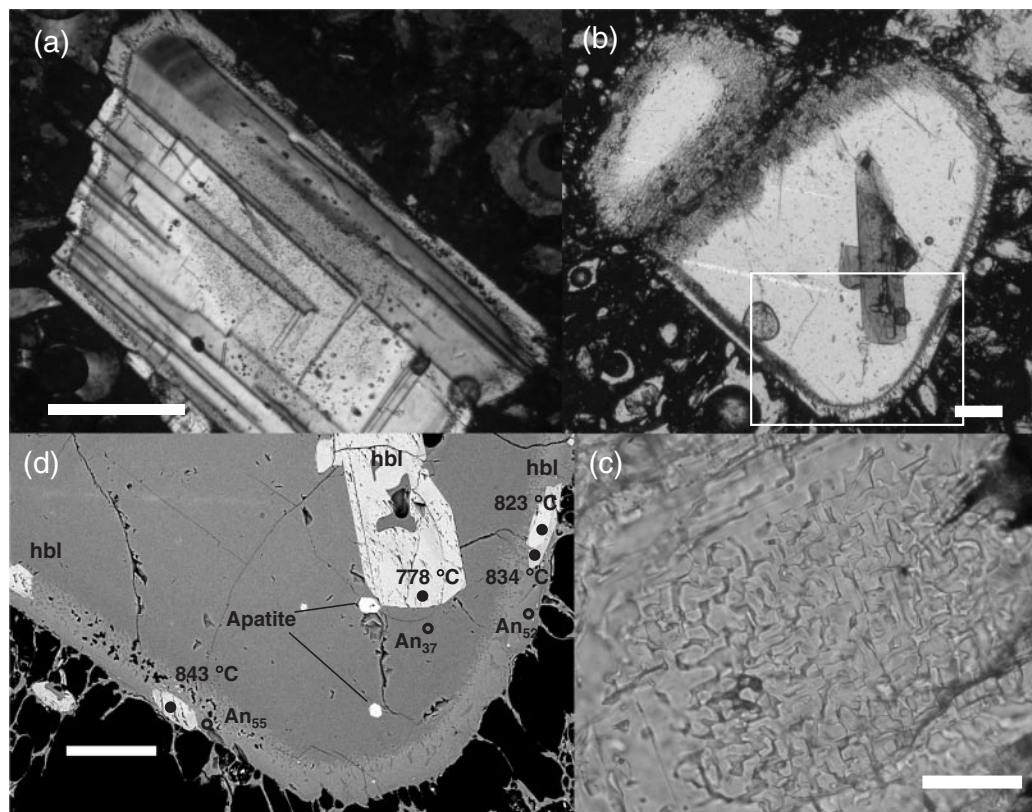
Fig. 9. Petrographic features of sieve-textured plagioclase. Some sieve plagioclase crystals have oscillatory zoned cores (a). The sieve texture comprises a network of micrometre-scale melt channels at the boundary between core and rim. This zone is usually a ring (b) but can exist throughout the interior (c). Backscattered SEM enlargement photograph of area indicated in (b) shows variation of plagioclase compositions (open circles) and temperatures calculated from coexisting hornblende (filled circles) (d). Scale bars represent 200 μm (a), 100 μm (b, d) and 50 μm (c).

1000 ppm Ba and 700 ppm Sr to approximately 400 ppm Ba and 200 ppm Sr (Fig. 17a). Ba and Sr concentrations in the melt then remain constant at these values while the Ab-rich plagioclase crystallizes. The early, decreasing trend is consistent with evolution of the melt during fractional crystallization of plagioclase (An_{62}) + hornblende + phlogopite ± pyroxenes (Fig. 17a). This assemblage is consistent with the mineralogy of cumulate xenoliths, and with the whole-rock data, which require involvement of a K-rich mineral (see Fig. 3). These early formed plagioclase crystals are then partially resorbed, forming the irregular cores. The residual melt following the early fractional crystallization stage has similar trace element chemistry to the later melt that crystallized the Ab-rich plagioclase infill. This lack of variation in melt chemistry implies that the patchy texture develops in response to an external factor such as P, T or pH_2O.

In the absence of varying melt composition, variations in X_{An} can be produced by varying any of temperature, pressure and pH_2O (e.g. Housh & Luhr, 1991). We used the plagioclase–liquid thermometer (Putirka, 2005) to assess the range of T, pH_2O conditions that could

produce the observed X_{An}. In these calculations, the external melt composition (i.e. the major element content of the coexisting liquid, a melt inclusion) is constant. The compositions of the host patchy plagioclase and adjacent melt inclusions were used to calculate T and pH_2O variations. For a given melt inclusion (liquid) composition and H_2O content, X_{An} increases with temperature, whereas for a given plagioclase–liquid compositional pair, H_2O in the liquid increases as temperature decreases. At constant pH_2O, a small temperature decrease (e.g. $\Delta T < -30°C$) is required to move from early, An-rich to late, albitic plagioclase for a typical plagioclase–liquid pair (Fig. 18). Conversely, at constant T, large changes in pH_2O (e.g. $\Delta P \sim -40$ MPa) are required (Fig. 18), equating to significant changes in depth. A positive ΔT is also possible, but ΔpH_2O must be even larger (Fig. 18). These calculations show that patchy textures in plagioclase develop during conditions of decreasing temperature or decreasing pH_2O.

These conditions are consistent with textural indications of partial resorption, if the magma is initially undersaturated with respect to H_2O. This is because significant resorption can occur during ascent of
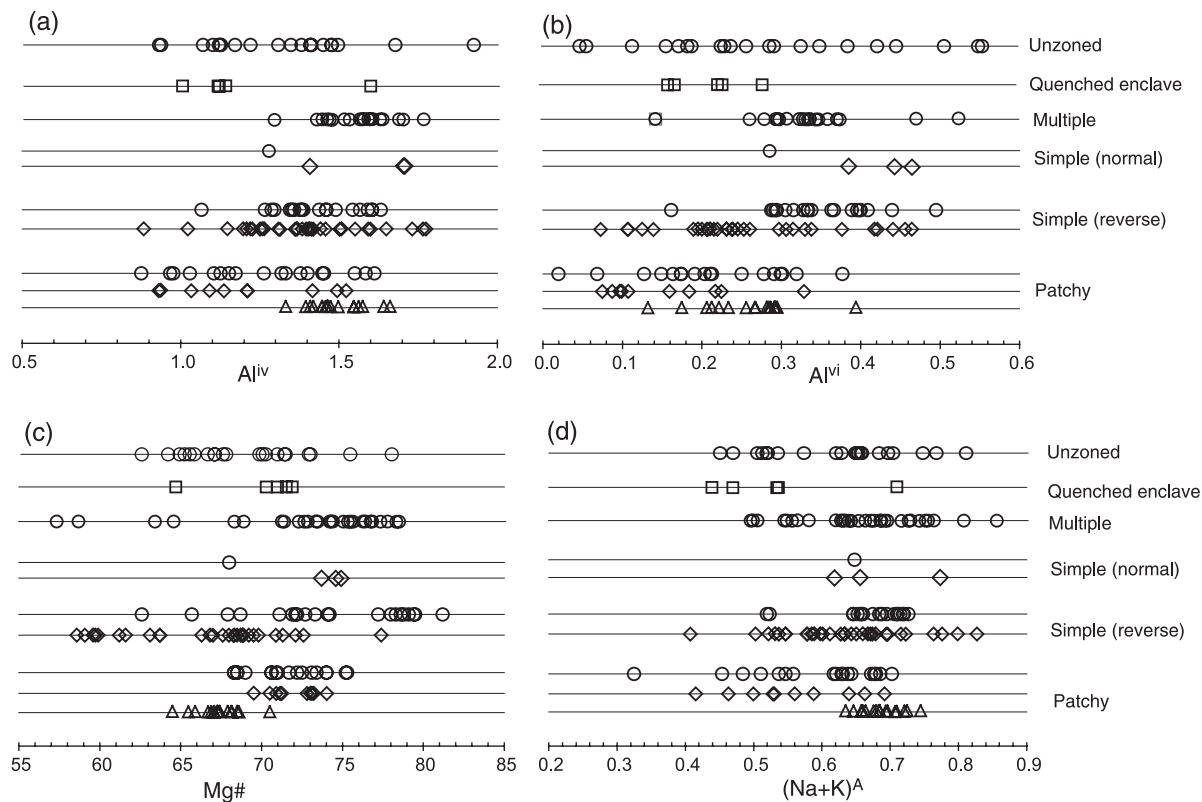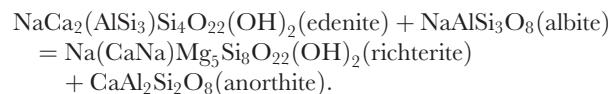
Fig. 10. Al^{vi}, Al^{vi}, Mg-number and $(Na,K)^A$ compositions of hornblende textural types. For simple and patchy zoning, circles represent rim compositions, and core compositions are represented by diamonds, or diamonds (dark) and triangles (bright) for patchy zoning.

H_2O-rich, but undersaturated, magmas (e.g. Holtz & Johannes, 1994; Johannes & Holtz, 1996; Clemens *et al*, 1997; Holtz *et al.*, 2001; Annen *et al.*, 2006). During adiabatic ascent, the melt fraction of the magma increases as a result of resorption (see Holtz & Johannes, 1994, fig. 7), and temperature changes are small ($\sim -70°C/GPa$; Annen *et al.*, 2006). As the magma rises, aH_2O will increase until the magma becomes H_2O-saturated. Thereafter, exsolution of H_2O will occur as the magma continues to decompress, causing crystallization of Ab-rich plagioclase once the melt crosses its liquidus (Annen *et al.*, 2006).

Patchy zoning in hornblende

The textural similarity between patchy plagioclase and hornblende (see Fig. 8) suggests a common resorption origin. Bright (late crystallizing) hornblende compositions have higher Al^{iv} and $(Na,K)^A$, but lower Mg-number than the earlier (Mg-rich, Al-poor) hornblende (Fig. 16b). Experimental studies indicate that this is consistent with crystallization of the later, Al-rich hornblende from a hotter melt (Scaillet & Evans, 1999; Rutherford & Devine, 2003). However, patchy plagioclase compositions indicate that temperatures

changes are small, and that resorption is driven by changing pH_2O (see Fig. 18). An alternative explanation is therefore that the composition of hornblende crystallizing is modified in response to the changing plagioclase composition. For example, decreasing pH_2O in the melt at constant T promotes crystallization of Ab-rich plagioclase (Fig. 18). Hornblende is thus driven to more Al-rich compositions, reflecting the edenite–richterite compositional exchange (Holland & Blundy, 1994):

$$NaCa_2(AlSi_3)Si_4O_{22}(OH)_2(edenite) + NaAlSi_3O_8(albite)$$
$$= Na(CaNa)Mg_5Si_8O_{22}(OH)_2(richterite)$$
$$+ CaAl_2Si_2O_8(anorthite).$$

This explanation requires Al-rich hornblende to coexist with albitic plagioclase (An_{29-54}), and Al-poor hornblende to coexist with anorthitic plagioclase (An_{42-74}), without significant temperature changes. Hornblende–plagioclase thermometry shows that pairs of patchy hornblende compositions can coexist with pairs of patchy plagioclase compositions, at temperatures that agree within error. Larger changes in X_{An} require a greater shift in hornblende Al_2O_3. Changes in plagioclase composition, as a result of changing pH_2O
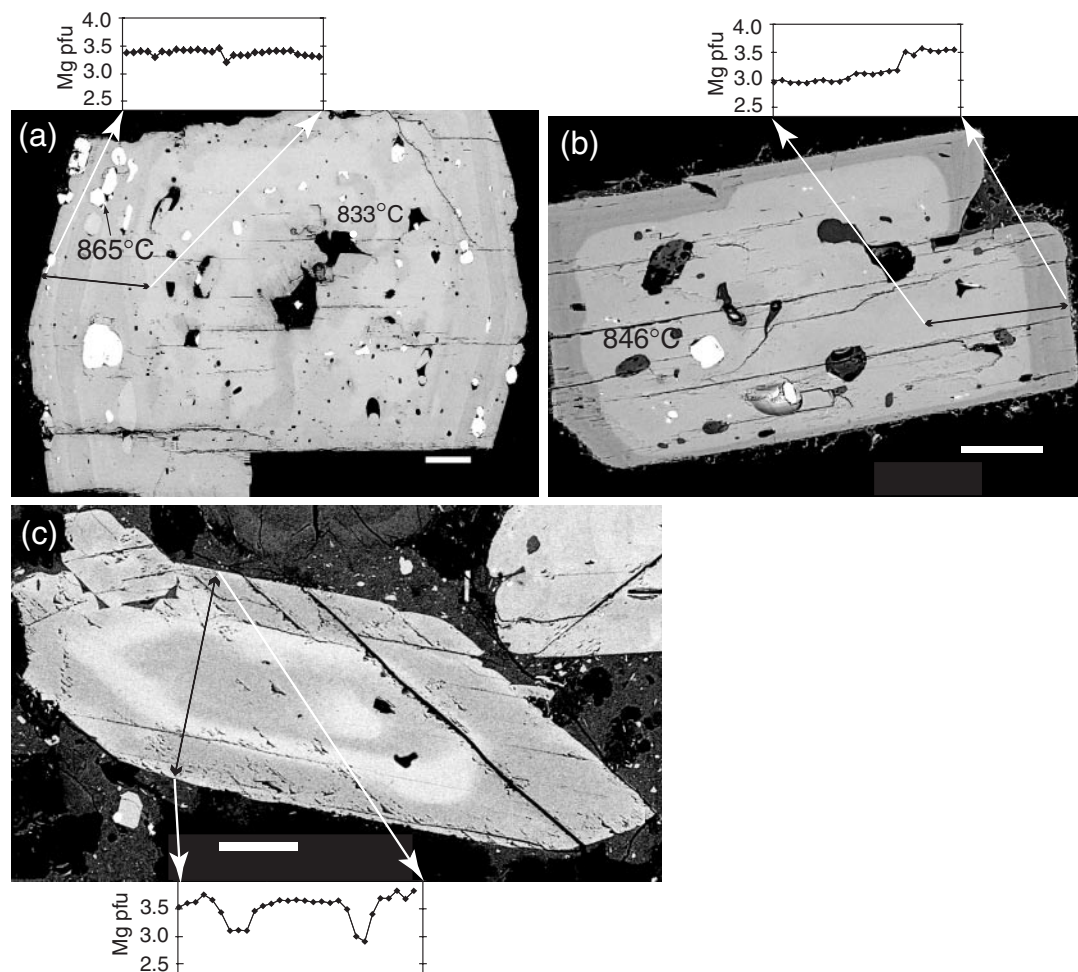
Fig. 11. Simple (a), patchy (b) and multiple zoning (c) in hornblende phenocrysts. Mg contents are shown for a profile across each crystal, calculated as atoms per formula unit (pfu). Black, double-ended arrows mark the line of each profile. Temperatures from hornblende–plagioclase or Fe–Ti oxide geothermometry are marked at relevant points. Scale bar represents 100 μm. Patchy phenocrysts comprise a core of dark and light patches, overgrown by a euhedral, oscillatory zoned rim. Simple-zoned phenocrysts have a distinct, Mg-rich rim composition, separated from the core by a sharp boundary. Multiple zoned phenocrysts have distinct, diffuse, Mg-poor (bright) zones.

at near-constant T, can therefore cause the observed variations in hornblende composition.

Summary

Textures and compositions of patchy plagioclase indicate resorption as a result of H_2O-undersaturated, adiabatic decompression (Fig. 16a). The textural similarity of patchy hornblende (Fig. 16b) suggests that a similar mechanism causes resorption of hornblende. The crystals originate at depth in an H_2O-rich, but undersaturated magma. Resorption occurs during adiabatic ascent as a result of superheating relative to the liquidus (Annen *et al.*, 2006). When crystallization recommences, H_2O contents in the magma are lower as a result of degassing, and the temperature may also be lower

because of adiabatic cooling and the heat of resorption. This results in crystallization of Ab-rich plagioclase and entrapment of melt inclusions. The composition of the accompanying hornblende therefore becomes more Al-rich. Thus crystallization under water-saturated conditions produces the observed patchy textures in plagioclase and hornblende. The origin of resorbed phenocrysts has been attributed to restite from partial melting (Raia & Spera, 1997) or cumulate material (Dungan & Davidson 2004; Annen *et al.*, 2006). At Shiveluch, falling Ba in the melt during crystallization of An-rich patchy plagioclase (see Fig. 17a) and K_2O variations in whole-rocks (see Fig. 3b) suggest some earlier crystallization of phlogopite. Inclusions of phlogopite occur in both plagioclase and hornblende phenocrysts, and phlogopite is also observed in cumulate

Table 4: Representative compositions and structural formulae of patchy, simple and other hornblende phenocryst types

	Patchy hornblende									Quenched enclave hornblende				
Grain:	m10s42			m10s44			m15s411			shiv013-27-2	shiv013-37-2	shiv013-7-11	shiv013-7-12	shiv013-7-15
Position:	Bright	Dark	Rim	Bright	Dark	Rim	Bright	Dark	Rim					
SiO_2	44·29	46·23	46·80	44·37	47·48	48·64	43·02	47·63	47·01	47·44	47·41	47·30	46·63	42·33
TiO_2	2·34	1·59	1·79	1·77	1·31	1·33	1·88	1·73	2·00	1·82	1·81	1·54	1·65	2·38
Al_2O_3	9·49	8·29	7·69	9·99	7·62	7·38	10·78	7·21	7·55	7·49	7·49	7·97	6·96	10·51
FeO	12·49	12·02	11·51	13·28	11·62	11·24	13·05	11·03	11·27	11·33	11·51	11·65	11·16	13·00
MnO	0·28	0·29	0·30	0·34	0·36	0·35	0·33	0·33	0·32	0·34	0·35	0·30	0·32	0·32
MgO	14·26	15·16	15·59	13·95	15·89	15·34	14·95	17·24	16·92	16·09	16·05	15·80	14·69	13·17
CaO	11·44	11·34	11·39	11·34	11·26	10·73	11·33	11·12	11·19	11·21	11·01	11·28	11·20	11·24
K_2O	0·48	0·34	0·33	0·5	0·31	0·37	0·49	0·31	0·32	0·30	0·31	0·29	0·29	0·44
Na_2O	2·09	1·84	1·78	2·03	1·67	1·72	2·21	1·70	1·79	1·77	1·75	1·73	1·55	2·13
Total	97·16	97·10	97·18	97·57	97·52	97·10	98·03	98·29	98·37	97·81	97·71	97·89	94·46	95·53
Mg-no.	0·67	0·71	0·70	0·70	0·71	0·72	0·69	0·74	0·73	0·73	0·72	0·72	0·71	0·65
Si T	6·553	6·790	6·848	6·553	6·790	7·065	6·341	6·863	6·789	6·882	6·887	6·862	6·998	6·406
Al T	1·447	1·210	1·152	1·447	1·210	0·935	1·659	1·137	1·211	1·118	1·113	1·138	1·002	1·594
	8·00	8·00	8·00	8·00	8·00	8·00	8·00	8·00	8·00	8·00	8·00	8·00	8·00	8·00
M1-3 Al	0·207	0·225	0·174	0·292	0·225	0·328	0·213	0·087	0·075	0·162	0·170	0·225	0·230	0·281
M1-3 Ti	0·260	0·176	0·197	0·197	0·176	0·145	0·208	0·187	0·217	0·198	0·198	0·168	0·186	0·271
M1-3 Fe^{3+}	0·538	0·607	0·633	0·483	0·607	0·538	0·452	0·602	0·578	0·459	0·476	0·657	0·429	0·584
M1-3 Cr	0·006	0·005	0·005	0·005	0·005	0·006	0·007	0·005	0·004	0·004	0·002	0·004	0·001	0·000
M1-3 Mg	3·145	3·319	3·400	3·071	3·319	3·321	3·283	3·704	3·642	3·479	3·474	3·417	3·286	2·970
M1-3 Fe^{2+}	0·844	0·669	0·592	0·834	0·669	0·661	0·837	0·415	0·484	0·698	0·680	0·530	0·867	0·893
	5·00	5·00	5·00	4·88	5·00	5·00	5·00	5·00	5·00	5·00	5·00	5·00	5·00	5·00
M4 Ca	1·813	1·784	1·786	1·794	1·784	1·670	1·789	1·717	1·731	1·742	1·713	1·754	1·801	1·822
M4 Fe^{2+}	0·146	0·110	0·214	0·000	0·110	0·110	0·169	0·283	0·269	0·204	0·228	0·207	0·092	0·147
M4 Mn	0·035	0·036	0·000	0·000	0·036	0·043	0·041	0·000	0·000	0·042	0·042	0·037	0·040	0·031
M4 Na	0·006	0·070	0·000	0·206	0·070	0·178	0·001	0·000	0·000	0·012	0·017	0·002	0·067	0·000
	2·00	2·00	2·00	2·00	2·00	2·00	2·00	2·00	2·00	2·00	2·00	2·00	2·00	2·00
A K	0·091	0·064	0·062	0·094	0·064	0·069	0·092	0·056	0·059	0·056	0·058	0·053	0·055	0·085
A Na	0·594	0·454	0·505	0·376	0·454	0·307	0·632	0·474	0·501	0·485	0·476	0·484	0·383	0·625
A site total	0·684	0·518	0·567	0·470	0·518	0·375	0·723	0·530	0·560	0·541	0·534	0·537	0·439	0·710

Table 4: continued

Grain:	Simple zoned hornblende						Multiple-zoned hornblende					
	shv2-26		m10s416		shiv013-23		sh18-9			shv2-13		
Position:	Core	Rim	Core	Rim	Core	Rim	Bright	Dark	Rim	Bright	Dark	Rim
SiO$_2$	44·80	46·65	44·09	45·30	45·26	45·07	45·27	45·45	45·64	44·24	45·64	46·55
TiO$_2$	1·58	1·10	2·39	1·56	2·10	1·62	1·12	1·25	1·27	1·55	1·52	1·65
Al$_2$O$_3$	9·54	9·32	9·19	8·97	9·34	10·37	11·53	11·18	10·37	11·96	12·81	8·45
FeO	14·28	7·55	14·40	14·28	13·15	11·06	12·61	9·24	9·58	11·31	8·94	10·14
MnO	0·34	0·10	0·34	0·40	0·30	0·16	0·25	0·15	0·17	0·22	0·12	0·24
MgO	13·47	17·92	12·90	13·34	14·97	15·90	12·89	16·93	16·34	13·89	14·86	16·50
CaO	11·25	11·81	11·12	10·92	11·08	11·27	11·28	10·52	11·34	11·38	11·28	11·51
K$_2$O	0·54	0·17	0·71	0·55	0·50	0·23	0·37	0·37	0·38	0·42	0·41	0·27
Na$_2$O	1·83	2·24	1·84	1·75	2·12	2·32	2	2·45	2·06	2·24	2·37	1·96
Total	97·64	96·86	96·98	97·07	98·80	98·00	97·43	97·59	97·28	97·24	97·99	97·29
Mg-no.	0·64	0·87	0·62	0·64	0·70	0·81	0·65	0·77	0·76	0·70	0·76	0·76
Si T	6·632	6·941	6·595	6·734	6·588	6·742	6·710	6·471	6·531	6·483	6·536	6·766
Al T	1·368	1·059	1·405	1·266	1·412	1·258	1·290	1·529	1·469	1·517	1·464	1·234
	8·00	8·00	8·00	8·00	8·00	8·00	8·00	8·00	8·00	8·00	8·00	8·00
M1-3 Al	0·297	0·575	0·216	0·305	0·190	0·570	0·683	0·348	0·281	0·548	0·697	0·214
M1-3 Ti	0·176	0·123	0·269	0·174	0·230	0·182	0·122	0·134	0·137	0·170	0·163	0·180
M1-3 Fe^{3+}	0·690	0·503	0·535	0·629	0·462	0·462	0·440	0·557	0·616	0·469	0·388	0·624
M1-3 Mg	2·973	3·763	2·876	2·956	3·247	3·546	2·788	3·593	3·485	3·034	3·170	3·575
M1-3 Fe^{2+}	0·862	0·000	1·102	0·935	0·869	0·239	0·957	0·362	0·467	0·776	0·575	0·403
M1-3 Mn	0·000	0·000	0·000	0·000	0·000	0·000	0·000	0·000	0·000	0·000	0·000	0·000
	5·00	5·00	4·92	5·00	5·00	5·00	5·00	5·00	5·00	5·00	5·00	5·00
M4 Ca	1·785	1·883	1·782	1·739	1·728	1·807	1·754	1·605	1·739	1·786	1·730	1·793
M4 Fe^{2+}	0·190	0·117	0·143	0·187	0·076	0·193	0·134	0·181	0·064	0·127	0·098	0·189
M4 Mn	0·025	0·000	0·043	0·050	0·037	0·000	0·031	0·018	0·021	0·028	0·014	0·018
M4 Na	0·000	0·000	0·032	0·023	0·159	0·000	0·081	0·196	0·176	0·059	0·158	0·000
	2·00	2·00	2·00	2·00	2·00	2·00	2·00	2·00	2·00	2·00	2·00	2·00
A K	0·103	0·032	0·135	0·104	0·092	0·043	0·069	0·067	0·069	0·079	0·074	0·050
A Na	0·525	0·647	0·502	0·481	0·439	0·673	0·482	0·480	0·396	0·410	0·230	0·622
A site total	0·628	0·678	0·637	0·585	0·531	0·715	0·551	0·547	0·465	0·489	0·304	0·672

Typical 1 S.D. are: SiO$_2$ ±0·1; TiO$_2$ ±0·16; Al$_2$O$_3$ ±0·1; FeO* ±0·1; MnO ±0·05; MgO ±0·35; CaO ±0·08; Na$_2$O ±0·03; K$_2$O ±0·05.
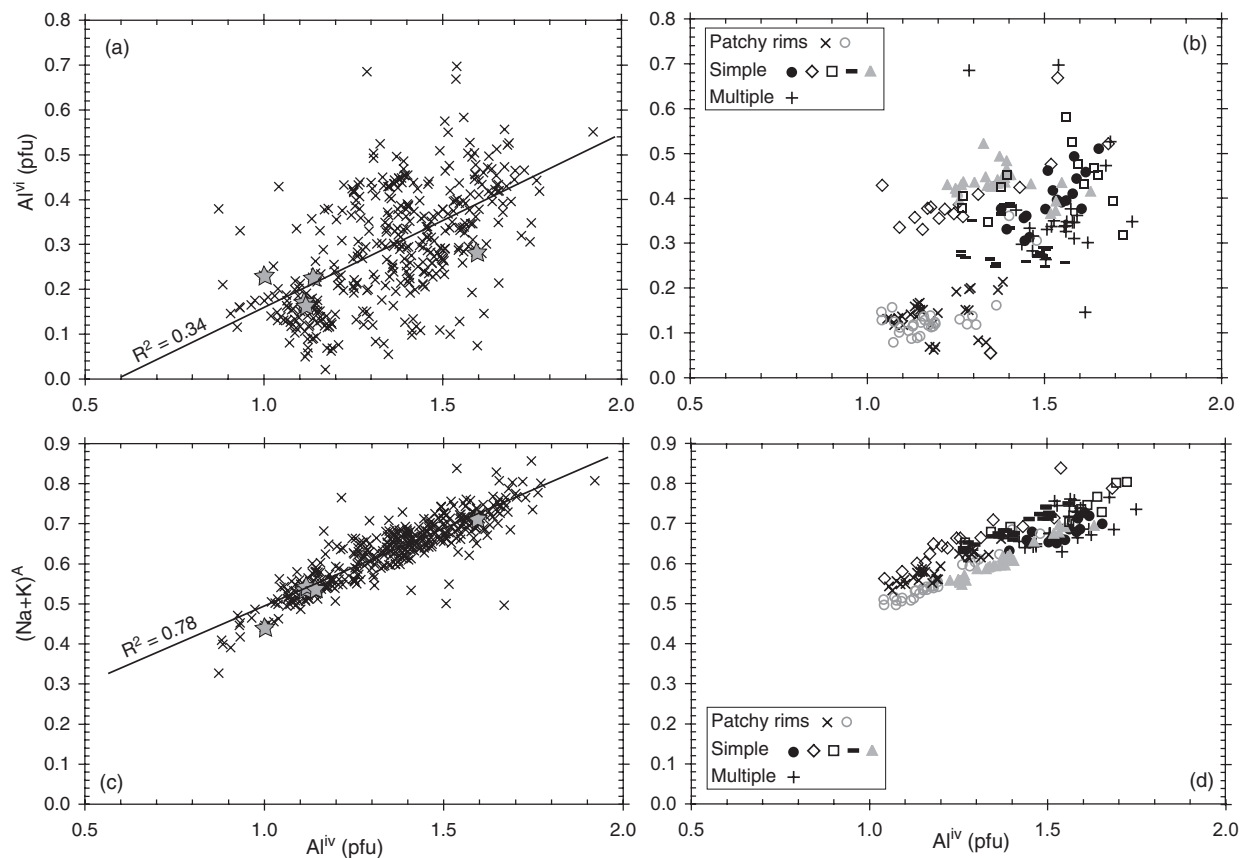
Fig. 12. Chemical variation in hornblendes. (a) Extent of Tschermak relationship (Al^{iv} vs Al^{vi}) for the whole dataset ($n = 420$) and (b) for multiple analyses on individual phenocrysts. Rims of patchy crystals tend to show lower Al^{iv} and Al^{vi} than simple or multiple zoned phenocrysts, suggesting crystallization at lower pressure. (c) Edenite exchange (Al^{iv} vs $(Na,K)^A$) for the whole dataset and (d) for multiple analyses on individual phenocrysts. The correlation is stronger than in (a), particularly within a given phenocryst, and is stronger for the rims of patchy phenocrysts than for other zoning types. Grey stars mark analyses from quenched enclave.

xenoliths. We infer that phlogopite was a stable phenocryst phase early in the magmatic history, possibly during prolonged fractional crystallization of basalts at high pH_2O in a crustal hot zone (Annen *et al.*, 2006). We therefore suggest, following Annen *et al.* (2006), that the patchy zoned plagioclase and hornblende phenocrysts are derived ultimately from cumulates or the high-P crystallization products of magmas.

Changes in oxygen fugacity

Compositional zoning in both hornblende (simple and multiple zoning) and apatite can be explained by changes in the oxygen fugacity of the melt. In this section we use experimental constraints to match compositional changes in hornblende and apatite to changes in external parameters (P, T, fO_2), because the lack of trace element variation suggests that the melt composition did not change significantly.

The composition of hornblende responds to P, T, fO_2 and pH_2O, as described by Scaillet & Evans (1999). In their experiments on the Mount Pinatubo dacite, a magma very similar in bulk composition, mineralogy and oxygen fugacity to the Shiveluch andesite, temperature increases caused increased Al_{tot}, Na_2O and TiO_2 of hornblende. The behaviour of hornblende Mg-number with changing temperature is ambiguous: Scaillet & Evans (1999) reported that Mg-number increases slightly with temperature, but this was contradicted by Rutherford & Devine (2003). We therefore assume that the effect of temperature on Mg-number is small. In contrast, Mg-number is strongly increased at higher fO_2 (Scaillet & Evans, 1999), because the activity of Fe^{2+} in the melt is reduced (Czamanske & Wones, 1973).

Simple zoning in hornblende is characterized by a sharp increase in Mg-number, Na and Si, and decrease in Ti from the core to the rim (Fig. 16c). The cores also show slowly decreasing Al^{iv}, Na^A and Ti, mirrored by a small increase in Mg-number (see Fig. 14). This pattern
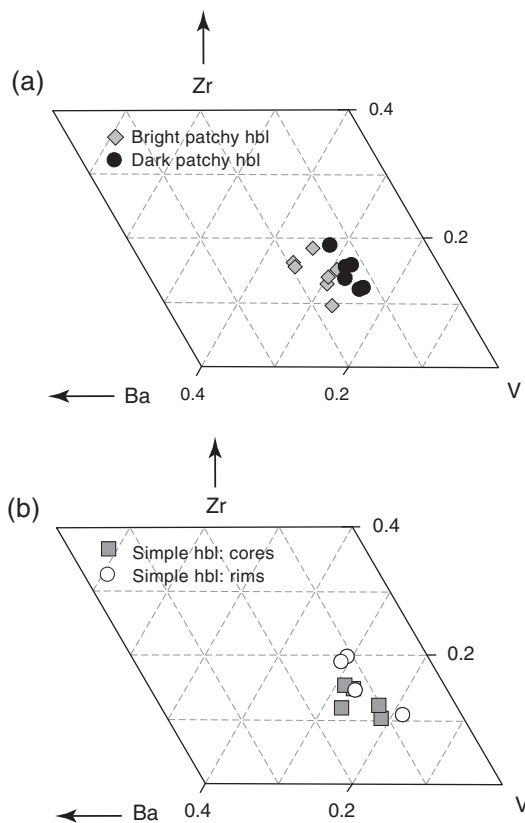
Fig. 13. Ternary diagram for trace elements Zr–Ba–V in (a) patchy hornblende and (b) simple hornblende. (a) Bright, Al-rich hornblende is slightly more Ba-rich than the dark, Al-poor hornblende, which has more V. (b) Simple cores and rims are virtually indistinguishable in terms of trace elements.

is consistent with gradual cooling during crystallization of the core (Bachmann & Dungan, 2002) followed by an increase in melt fO_2 during rim crystallization. The (rare) normally zoned hornblende phenocrysts show a decrease in rim Mg-number. They are therefore inferred to have undergone a reduction in oxygen fugacity. The magnitude and nature of the compositional variations correspond well in simple- and multiple-zoned hornblende (Fig. 16c and e), suggesting that a similar mechanism causes both zoning types.

In apatite, zoning is most clearly seen in S. Apatite, $Ca_5(PO_4)_3(OH,Cl,F)$, incorporates sulphur by partial replacement of PO_4^{3-} by SO_4^{2-}. High sulphur contents in apatite are generated by high oxygen fugacity, because S^{6+} (SO_4^{2-}) is stabilized, and by high melt sulphur contents (e.g. Peng et al., 1997). The effect of increasing temperature on sulphur contents in apatite is unclear: recent studies cite both increasing (Parat & Holtz, 2004) and decreasing (Peng et al., 1997) sulphur in apatite. Normal zoning in apatite could therefore be explained either by the melt becoming enriched in S, or by an increase in oxygen fugacity (Peng et al., 1997; Parat &

Holtz, 2004). Apatite in the quenched enclave is more S-rich than apatite in the host andesite (see Fig. 15). However, fO_2 in the quenched enclave is the same as that of the host andesite (see Fig. 4). This suggests that the high sulphur contents in apatite result from high melt sulphur, not high fO_2.

Magma recharge

The xenocrysts of olivine and orthopyroxene, characterized by their Mg-rich compositions, strong normal zoning, well-developed reaction rims (olivine) or overgrowth rims (orthopyroxene), and inclusions of chromite (olivine), are clear indications of recharge of the andesite by a more mafic magma (e.g. Sakuyama, 1984; Clynne & Borg, 1997). Using the widths of reaction rims surrounding olivine, Dirksen et al. (2006) constrained residence times of olivines in the andesite magma to between 2 months and 4 years, suggesting that mafic recharge occurred both shortly before and during the 2001–2004 eruption.

Mixing with felsic magma

As well as the presence of xenocrysts, zoning in phenocrysts can be used to detect the influx of a new magma. Sieve plagioclase phenocrysts (Fig. 16d) are observed at many arc volcanoes, and the texture is commonly attributed to reaction between the plagioclase and a melt in which more An-rich plagioclase is in equilibrium (e.g. Tsuchiyama, 1985; Nakamura & Shimakita, 1998). This melt could be more mafic, or hotter, or both. A change in minor and trace elements between the sieve plagioclase core and rim would indicate a change in melt composition (Singer et al., 1995); heating alone would not affect minor and trace element concentrations except through changes to the partition coefficients. We calculated Ba and Sr contents of melts coexisting with the sieve plagioclase (Fig. 17b), using the same method as for the patchy plagioclase. The calculations indicate that the melt in equilibrium with the rims was richer in Ba and Sr than that in equilibrium with the cores (Fig. 17b). This indicates that sieve plagioclase rim crystallization occurred in a hotter, more mafic melt than core crystallization. This interpretation is supported by higher values of Mg, Fe and X_{An} in sieve plagioclase rims (see Table 3 and Fig. 5), and higher temperatures as calculated by geothermometry (see Fig. 9d). The variable width of the sieved region is probably related to the degree of disequilibrium experienced by an individual crystal (Clynne, 1999). However, the sieved cores probably come from a more felsic magma that mixed with the host andesite, because the cores are albitic and Fe-poor compared with most plagioclase phenocrysts (Fig. 5).
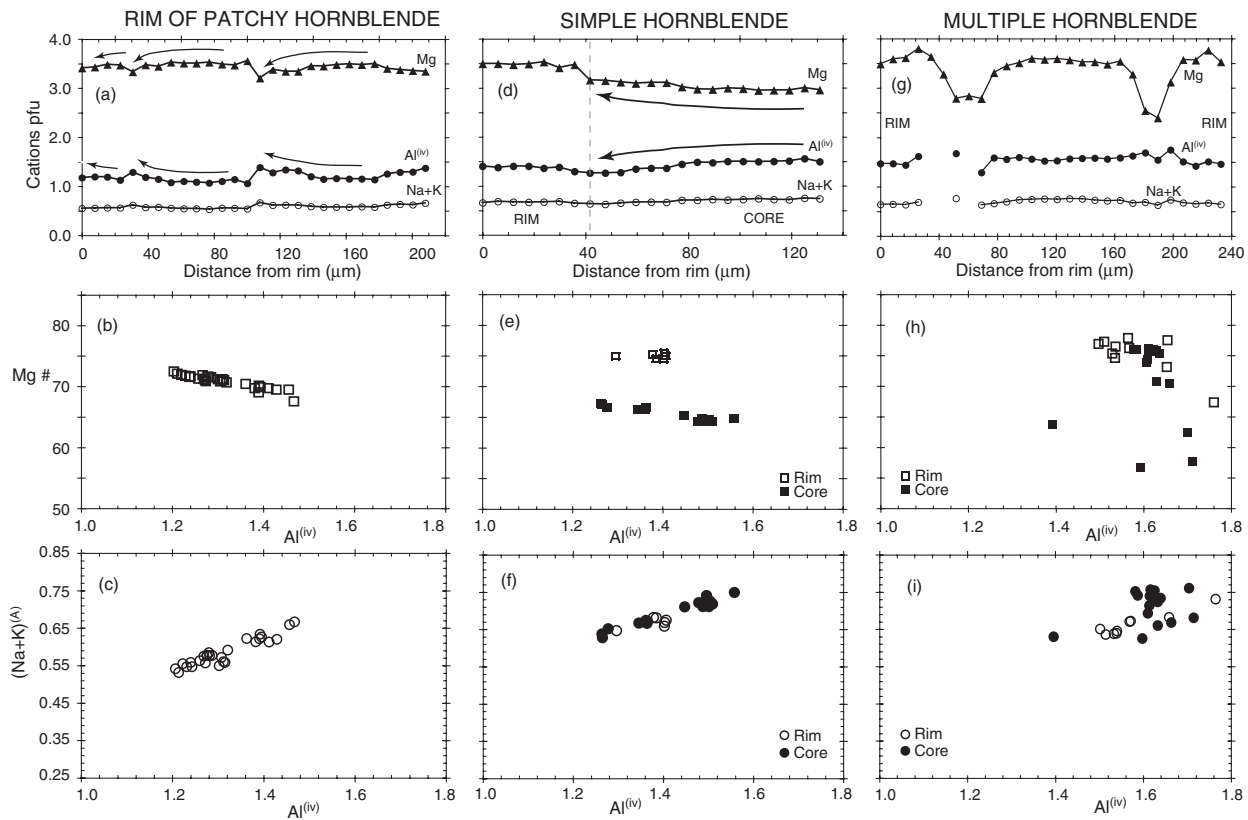
Fig. 14. Chemical zoning information from different hornblende phenocryst types. In each panel, the top figure shows a zoning profile with structural elements reported as cations per formula unit (pfu). Curved arrows highlight zoning patterns. The middle figure shows variation of Mg-number with Al^{iv}. The bottom figure shows variation of $(Na + K)^A$ with Al^{iv}. Open symbols represent rim compositions; filled symbols represent cores. Typical errors are given where they are greater than the size of the symbols. (a–c) Rim of patchy hornblende phenocryst. Rims show good correlation of Mg-number vs Al^{iv}, and Al^{iv} vs $(Na + K)^A$, and fine oscillatory zoning. (d–f) Simple hornblende phenocryst. Rims have markedly higher Mg-number than cores. (g–i) Multiple zoned hornblende shows poor correlation between $(Na + K)^A$ and Al^{iv}. Zones involve large jumps in Mg-number.
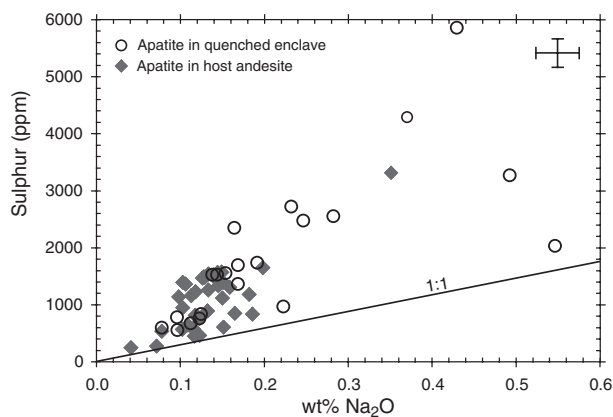
Fig. 15. Sulphur and Na contents of apatites from host andesite (filled diamonds) and from the quenched enclave (open circles). Very S-rich apatites are much more common in the quenched andesite. 1:1 line indicates atomic substitution of S^{6+} for Na^+. Error bars indicate typical 1 S.D. from EPMA counting statistics.

Mixing with mafic magma

The quench texture of the andesite enclave gives a clue to the zoning observed in both hornblende and apatite. To summarize, quenching is indicated by the large amounts (∼15%) of microlite-free, vesicular glass (e.g. Eichelberger, 1980), by the acicular habit of apatite (Wyllie *et al.*, 1962) and hornblende, and by dendritic extensions on some phenocryst and microphenocryst rims (see Fig. 2c and d). The composition of the interstitial glass is identical to that of the more evolved melt inclusions and matrix glasses in the host rock. Modal analysis suggests that the enclave bulk composition is slightly more mafic than the host silicic andesite. Estimated crystallization temperatures of the quenched enclave are consistent with those of the host magma (see Table 2). We propose the following sequence of events to explain these observations.

New basaltic-andesite melt, which was hotter and/or richer in dissolved volatiles (e.g. S) than the host andesite, intrudes the shallow magma storage region. The close
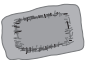
	Mineral	Zoning type	Texture	Features	Interpretation
a	Plagioclase	Patchy		Core: Partially resorbed; An-rich; low Ba; no changes in Fe, Mg Exterior: Ab-rich; texturally associated with melt inclusions; high Ba; oscillatory zoned rim. No changes in Fe, Mg	Core forms at high pH_2O during cumulate formation. Resorption occurs during H_2O-undersaturated decompression.
b	Hornblende	Patchy		Core: Irregular; partially resorbed; Al-poor; low Ba Exterior: Al-rich; texturally associated with melt inclusions; higher Ba; oscillatory zoned rim. Good correlation of Al^{iv} and $(Na,K)^A$	Core forms during cumulate formation. X_{An} (plag) decreases with pH_2O, causes change to Al-rich exterior. Resorption occurs during ascent.
c	Hornblende	Simple		Cores: Fairly uniform; Al^{iv} decreases rimward; higher V; low Mg, Na, Si Rim: Sharp change to high Mg, Na, Si; lower V; normal zoning is rare. Poor Al^{iv}-$(Na,K)^A$ correlation	Cores form during slight cooling. Abrupt increase in fO_2 causes rim formation.
d	Plagioclase	Sieve		Core: anhedral, Ab-rich, low Fe, low Mg. Rim: separated from core by layer of melt channels; An-rich, high Fe, high Mg	Sieve texture develops on mixing with more mafic melt.
e	Hornblende	Multiple		Composition very similar to simple hornblendes. Strong, diffuse zoning of Mg#. Poor Al^{iv}-$(Na,K)^A$ correlation.	Strong changes in fO_2, perhaps due to multiple degassing events? See text for discussion.
f	Apatite			Both normal and reverse zoning of S.	Mixing of andesite with high-S mafic andesite melt.
g	Plagioclase	Oscillatory		Core: Broad, diffuse zones Rim: Zoned: sharp boundaries to higher X_{An}, gradual decay. Consistent rim compositions; gradual Fe/Al increase; zones correlated with patchy plagioclase rims	Pulsatory changes in pH_2O and/or temperature during ascent. Increasing fO_2 during ascent results from H_2O degassing

Fig. 16. Summary of textures and chemical characteristics of phenocryst zoning.

similarity of temperature estimates and mineral and melt compositions of the enclave compared with those of the host magma suggests that the intruding magma was efficiently quenched, to a temperature very close to that of the host (Blundy & Sparks, 1992). This means that the intruding magma must be very small in volume compared with the volume of the host magma (Sparks & Marshall, 1986). Unlike many quenched inclusions, the edges of the enclave are defined by crystal margins, rather than a fine-grained chilled layer. This suggests that a rigid crystalline framework was present at its incorporation into the host. We infer that the enclave represents part of a larger inclusion that broke up in a semi-brittle fashion, although it is also possible that the intruding magma may have been already partially crystallized.

S contents in the melt of the enclave increase as crystallization occurs. This results in the formation of S-rich zones in apatite microphenocrysts (Fig. 16f) and the nucleation of anhydrite (Peng et al., 1997). Reversely zoned apatite crystals (Fig. 16f) are probably derived from the intruding magma and transferred into the host andesite. When the melt vesiculates, S partitions into the vapour phase with H_2O because the solubility of S in oxidized, silicic melt is low (Carroll & Rutherford, 1985). Anhydrite, which is abundant in the enclaves, comes into contact with the host magma as the enclaves break up, where it begins to dissolve, releasing O_2 and thus oxidizing the surrounding melt:

$$CaSO_4(s) + SiO_2(m) = CaSiO_3(s) + SO_2(g) + \frac{1}{2}O_2(g).$$

The nominal $CaSiO_3$ component is probably incorporated into hornblende or pyroxene. The Mg-rich zones of simple- and multiple-zoned hornblende (Fig. 16d and e) form under these more oxidizing conditions. It is possible that the rapid exsolution and vesiculation event in the intruding magma could also cause oxidation (Candela, 1986; Peng et al., 1997). We speculate that the rare, multiple-zoned hornblende phenocrysts may have undergone more than one oxidation event, perhaps during repeated injection or intricate mixing with the intruding andesite.

An important aspect of magma chamber evolution is highlighted by the mineralogy of the quenched enclave. The quenched enclave recorded crystallization temperatures of 808–836°C, equivalent to those of the host andesite (see Table 2). Crystallization at this temperature resulted in the assemblage plag + hbl + oxides + opx, which is different from the expected near-liquidus
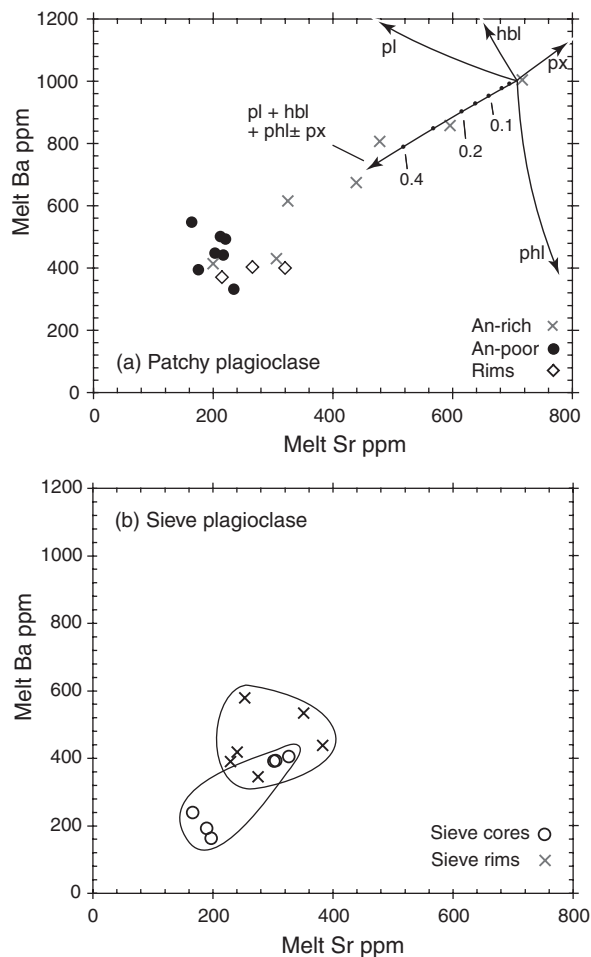
Fig. 17. (a) Melt Sr and Ba contents calculated to coexist with early (An-rich), late (Ab-rich) and rim compositions of patchy plagioclase. Melt composition changes strongly during crystallization of An-rich plagioclase, thereafter showing little variation. Arrows indicate melt evolution during crystallization of phenocryst phases. Partition coefficients are taken from Blundy & Wood (1991) for plagioclase (pl), Nash & Crecraft (1985) for phlogopite (phl) and Tiepolo *et al.* (2003) for hornblende (hbl). We assume that D_{Ba} and D_{Sr} in pyroxenes (px) are ~0·1. The melt starting composition is taken as ~700 ppm Sr and 1000 ppm Ba. The calculated melt variation requires fractionation of an assemblage of pl + hbl + phl ± px, in the approximate ratio 25:50:15:10. Tick marks indicate percent fractional crystallization. Typical errors from LA-ICP-MS analysis are the size of the symbols. (b) Melt Sr and Ba contents calculated to coexist with sieve plagioclase cores and rims, using partition coefficients calculated from Blundy & Wood (1991). Rims crystallized from a melt richer in Ba and Sr.

Fig. 18. Anorthite content of plagioclase, calculated as a function of temperature and pH$_2$O using Putirka (2005). The large changes in plagioclase composition (e.g. ~20 mol % anorthite) from earlier formed, An-rich plagioclase to later, albitic plagioclase can be produced by small temperature decreases (e.g. −25°C) or larger drops in pH$_2$O (e.g. −40 MPa).

including olivine and pyroxene to form. This would require a proportionally larger volume of intruding magma (Sparks & Marshall, 1986). In the latter case, clearly recognizable xenocrysts would form on break-up of enclaves. However, break-up of the hb–plag enclave described here would result in 'xenocrysts' indistinguishable, in terms of major elements, from primary phenocrysts.

These observations suggest that some sub-volcanic magma chambers may be kept 'topped up' by a continuous (over long time-scales) drip-feed of small parcels of magma that are derived from depth. At Shiveluch, the above discussion shows that there is evidence for intrusion of both more mafic and more felsic magmas. The process may be punctuated by the arrival of larger batches of mafic magma, injected shortly prior to or during eruption. The consequence of 'drip-feeding' very small parcels of magma into the system is that the major element composition of the residual liquid or melt will remain relatively constant because the residual liquids of the intruding magmas are close in composition (Fig. 19). In contrast, bulk-rock compositions may be drawn out towards the compositions of intruding magmas (Fig. 19) and by assimilation of cumulate material, as suggested in Fig. 3. We anticipate that, although the major element composition of the residual liquid remains relatively constant, this process may leave a trace element signature.

Oscillatory zoning

Various factors causing oscillatory zoning in plagioclase have been proposed, including kinetically or diffusion-

assemblage of perhaps ol + cpx + plag. Blundy & Sparks (1992) showed experimentally that when a magma is rapidly undercooled, the liquidus and near-liquidus assemblages are by-passed and only the low-T assemblage forms. Such efficient and rapid thermal equilibriation implies a very small volume of intruding magma relative to the volume of the host (Sparks & Marshall, 1986). In contrast, more prolonged crystallization at high temperatures would be needed for an assemblage
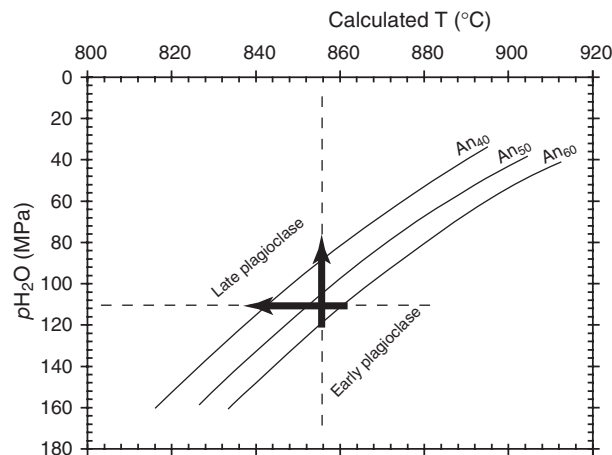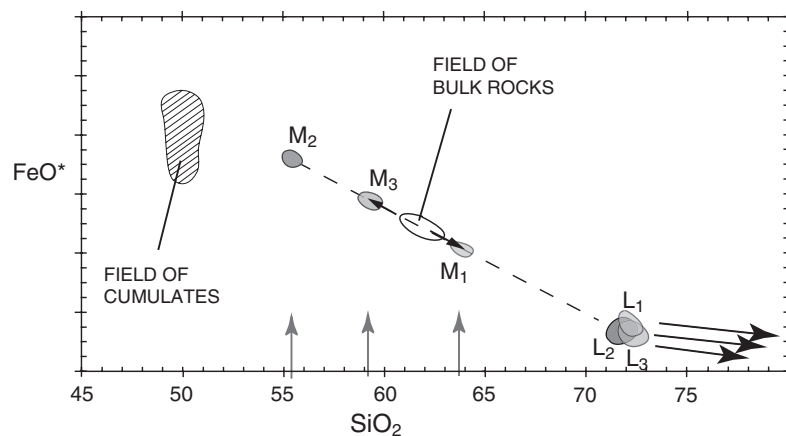
Fig. 19. Schematic diagram illustrating magma evolution during repeated injection of magmas of similar compositions, using FeO* as an example. Parcels of magma (e.g. M_1, M_2, M_3) are injected into the system. Their residual liquids are of similar compositions, probably rhyolitic (e.g. L_1, L_2, L_3) despite small differences in bulk SiO_2. This means that the compositions of the bulk residual liquid changes little, while the whole-rock compositions are drawn out to slightly more silicic or more mafic compositions. This process might be expected to leave a detectable trace element signature. Incorporation of remobilized cumulate material (cross-hatched region) may also drag the whole-rock compositions to more silica-poor compositions. The residual liquids evolve together in a similar manner (black arrows).

controlled growth (Bottinga *et al*, 1966; Allègre *et al.*, 1981; Pearce & Kolisnik, 1990), decompression (Nelson & Montana, 1992), repeated mafic recharge (Singer *et al.*, 1995), silicic recharge (Ginibre *et al.*, 2002), and magma convection (e.g. Singer *et al.*, 1995). Because small amounts of resorption are commonly associated with zoning (see Fig. 7), we consider that kinetic effects are unlikely, and that some change in external parameters produces the zoning. We concentrate here on the compositional zoning observed at the rims of oscillatory zoned plagioclase (Fig. 16g) and some patchy zoned plagioclase (Fig. 16a) phenocrysts. This zoning is characterized by resorption followed by abrupt increases in X_{An}, followed in turn by slower decay. The frequent, rhythmical oscillations suggest crystallization from a melt that was undergoing frequent, rhythmic changes in temperature or pH_2O. The zoning is underlain by gradually increasing Fe/Al.

Eruption dynamics

Recent work on numerical modelling of conduit flow processes (Melnik & Sparks, 2005) during decompression-driven crystallization showed that unstable magma flow regimes can cause periodic variations in magma discharge rate, and hence oscillatory pressure fluctuations within the magma chamber. In addition to the pressure oscillations, replenishment by more mafic material (as occurs at Shiveluch) can produce oscillatory temperature changes at the top of the conduit (Melnik & Sparks, 2005). Because the Shiveluch magma is H_2O-saturated (see below), variations in pressure would affect pH_2O of the magma. Because of the strong dependence of plagioclase X_{An} on

both pH_2O and T, the presence of unstable flow regimes provides a mechanism for the formation of oscillatory zoning in the rims of plagioclase phenocrysts. The pressure fluctuations can also explain the typical sharp increase in X_{An} and slower decay of the outer zones. As the pressure increases, plagioclase growth will slow and resorption may occur. The next zone will therefore begin by crystallizing An-rich plagioclase, and then decay back to more An-poor plagioclase.

To test this further, we used the plagioclase–liquid thermometer (Putirka, 2005) to estimate the ΔpH_2O or ΔT required to produce the observed X_{An} variation in the plagioclase zoning. X_{An} zoning ranges from 5 to 19 mol %, but is typically 9–15 mol % An. For a typical melt inclusion composition, this requires ΔpH_2O of approximately +16 to +26 MPa, or ΔT of approximately +6 to +13°C. At low pressures, typical values are ΔpH_2O of +3 to +7 MPa and ΔT of +8 to +15°C. These changes in pH_2O of a few megapascals are equivalent to large vertical movements (e.g. 650–1000 m, or 120–300 m at shallower pressures), so convection in the magma chamber is also a possible explanation. However, the temperature and pressure oscillations predicted from numerical modelling are ~7–20 MPa and ~60–80°C (Melnik & Sparks, 2005), and thus sufficient to account for the observed oscillatory zoning in plagioclase.

Decompression-driven crystallization

The model requires that magma ascent from the chamber is accompanied by decompression-driven crystallization. At Shiveluch, this is indicated by the volatile contents and compositions of melt inclusions,

which record the changing composition and volatile content of the evolving melt phase during crystallization of phenocryst rims and groundmass. The melt inclusions show a negative correlation of H_2O with SiO_2, and track towards the Qz–Or join on a H_2O-saturated haplogranite ternary diagram (Humphreys, 2006). These trends indicate H_2O-saturated, decompression-driven crystallization (Blundy & Cashman, 2001; 2005), in keeping with numerous recent studies reporting decompression-driven crystallization at andesitic and dacitic volcanoes, such as Montserrat (Sparks *et al.*, 2000), Mount St. Helens (Blundy & Cashman, 2005) and Unzen (Nishimura *et al.*, 2005).

The increasing Fe/Al in plagioclase rims can also be explained by H_2O-saturated, decompression-driven crystallization. Increasing Fe or X_{An} could reflect changes in melt chemistry. However, this seems unlikely because the highest Fe/Al values are observed at the outermost rim. Experimental data indicate that both D_{Fe} and Fe/Al in plagioclase increase with increasing fO_2 (Wilke & Behrens, 1999). We therefore ascribe increasing Fe and Fe/Al in plagioclase to gradually increasing oxygen fugacity during the late stages of crystallization. Candela (1986) showed that the release of aqueous vapour results in oxidation of the melt as a result of preferential loss of H_2. At Shiveluch, this is supported by observations that groundmass magnetite is concentrated near bubbles (P. Pletchov (2004), personal communication). We note that, because D_{Fe} also increases with T (Wilke & Behrens, 1999), it is possible that increasing Fe/Al could also result from rising temperatures as a result of release of latent heat during decompression-driven crystallization (Blundy *et al.*, 2006). Either way, the high Fe/Al in plagioclase phenocryst rims and groundmass plagioclase is consistent with crystallization driven by degassing of H_2O.

Prolonged history of crystallization

We now consider the origin of the diffuse, broad zones found in the cores of oscillatory zoned phenocrysts (Fig. 6). These are probably produced by a different mechanism compared with the narrower, sharp outer zones because they show an approximately inverse relationship between X_{An} and Fe/Al, which is not seen in the outermost zones (see Fig. 6). The diffuse nature of the core zoning implies long residence times to allow for slow CaAl–NaSi diffusion (Grove *et al.*, 1984). We therefore suggest that the cores of oscillatory zoned crystals represent the dominant crystal population resident in the chamber over long periods of time. The compositional zoning could result from regular inputs of fresh magma and continued slow growth as a result of cooling or degassing, whereas the rims reflect later growth. This interpretation is consistent with studies that

have shown a wide discrepancy between the ages of phenocryst cores and rims (e.g. Turner *et al.*, 2003). We suggest that the unzoned hornblendes also represent this resident crystal population.

Textural overlap between phenocrysts

We have tried to explain the textural variations between phenocrysts by relating them to processing occurring during ascent and mixing of separate batches of magma (Fig. 20). These processes include crystallization, remobilization and resorption of cumulates (patchy phenocrysts), breakdown of anhydrite during mixing of sulphur-rich magmas (apatite and hornblende), and mixing with mafic magmas, whether basalt or basaltic andesite. If different crystal populations share a textural feature (e.g. shared rims), this would imply that batches of crystals had a common crystallization environment for some length of time. In contrast, if there is no overlap between phenocryst types, the different crystal populations must be spatially or temporally isolated during crystallization. In the lavas studied, there is limited evidence of different textures overlapping between phenocryst populations. Most phenocryst populations tend to record a distinct and individual magmatic history, implying that they were mixed together very late or even during eruption. However, their close spatial relationship in the erupted samples suggests that crystals with different histories may not have been far apart in absolute distance (e.g. Kouchi & Sunagawa, 1985).

There are three cases where textural overlap does occur. First, oscillatory zoned cores are observed in some sieve plagioclase crystals (Fig. 9). Second, oscillatory zoned rims occur on patchy plagioclase cores (Figs 6 and 16a). Third, some patchy hornblende phenocrysts seem to have similar oscillatory zonations in their rims (see Fig. 14a). The occurrence of oscillatory zoning in patchy plagioclase rims indicates that the patchy phenocrysts experienced the same rhythmic fluctuations in temperature or pH_2O as the oscillatory phenocrysts. In our interpretation, this is because the patchy cores crystallized much earlier and were derived from cumulate material, but, after mixing, shared the later stages of crystallization with the oscillatory plagioclase. The oscillatory zoning in some hornblende rims may be a response to the same $P–T$ fluctuations. In contrast, sieve plagioclase crystals only show a single zone in the rim, but sometimes have oscillatory zoning in their cores. This implies that these sieve-textured crystals are rather younger than most other plagioclase crystals (i.e. they were mixed in even later in the magmatic history). Figure 20 illustrates schematically the possible spatial relationships between phenocryst populations.
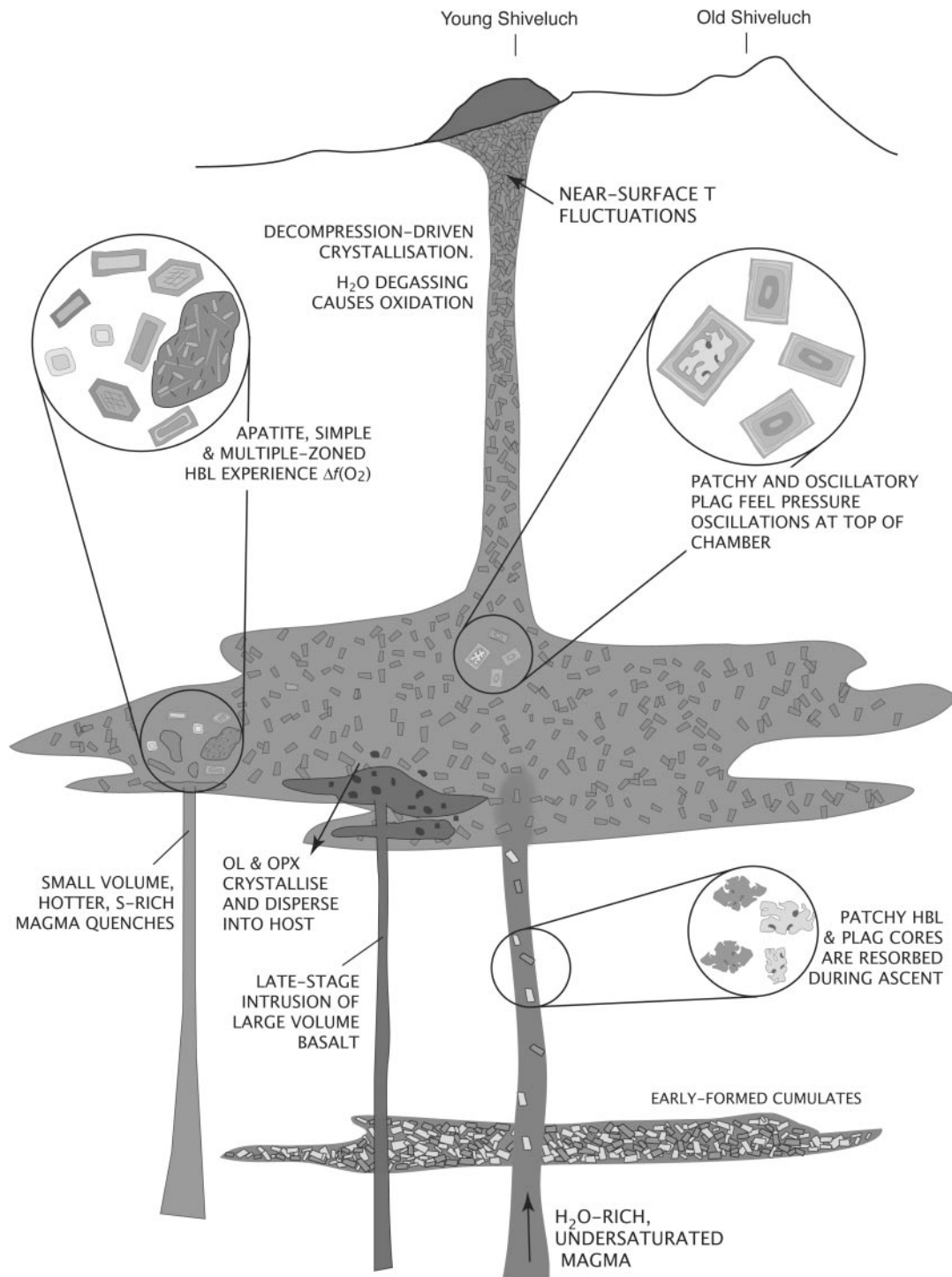
Fig. 20. Schematic diagram showing possible spatial relationships between different phenocryst zoning populations, and summarizing their mode of formation. Not to scale.

Our main temporal constraint on the time-scales of mixing comes from the lack of breakdown rims on hornblende phenocrysts. Work on the growth rate of amphibole breakdown rims suggests that this final mixing must take place over very short time-scales; that is, less than 5–6 days (Rutherford & Hill, 1993; Browne & Gardner, 2002). Even taking into account the much lower diffusivity of Si in a melt with 80 wt % SiO_2,

low H_2O and at lower temperatures, ascent times must still be of the order of 2–3 weeks (Buckley, 2003) to avoid hornblende breakdown. This implies that the last stages of crystallization occurred rapidly.

CONCLUSIONS

Andesites from Shiveluch Volcano contain petrological evidence for open-system magmatic processes. Patchy zoned hornblende and plagioclase phenocrysts represent high-pressure crystals or cumulates, remobilized as H_2O-undersaturated melts rise into the upper crust, and resorbed during ascent. When crystallization starts again, resorbed plagioclase cores are infilled and over-grown with more albitic plagioclase, driving hornblende to crystallize more Al-rich compositions. The magma chamber accumulates slowly, by intermittent addition of small volumes of magma, forming a dominant popula-tion of unzoned hornblende and oscillatory zoned plagioclase cores. The replenishing magmas vary in composition, including cooler silicic dacite and hotter mafic andesite, which forms enclaves rather than cryptic mixing. The crystallization temperature and mineralogy of the hotter magma are identical to those of the host andesite, indicating efficient heat transfer and thus small volumes of intruding magma. Differences in dissolved volatile contents between intruding magmas can result in significant geochemical zonation in hornblende and apatite.

Mg-rich orthopyroxene and olivine xenocrysts indicate late-stage influx of hotter magma from depth, causing chamber mixing contemporaneous with eruption. Decompression in the conduit during eruption leads to crystallization of plagioclase and other groundmass phases, accompanied by oxidation resulting from exsolution of H_2O. Oscillatory zonation in plagioclase may result from pressure and temperature oscillations in the subvolcanic plumbing system, related to instabilities in magma discharge rate.

ACKNOWLEDGEMENTS

REFERENCES

Allègre, C. J., Provost, A. & Jaupart, C. (1981). Oscillatory zoning: a pathological case of crystal growth. *Nature* **294**, 223–228.

Andersen, D. J., Lindsley, D. H. & Davidson, P. M. (1993). QUILF: a Pascal program to assess equilibria among Fe–Mg–Ti oxides, pyroxenes, olivine and quartz. *Computers and Geosciences* **19**, 1333–1350.

Anderson, A. T. (1976). Magma mixing: petrological process and volcanological tool. *Journal of Volcanology and Geothermal Research* **1**, 3–33.

Annen, C., Blundy, J. D. & Sparks, R. S. J. (2006). The genesis of intermediate and silicic magmas in deep crustal hot zones. *Journal of Petrology* **47**(3), 505–539.

Arculus, R. J. & Wills, K. J. A. (1980). The petrology of plutonic blocks and inclusions from the Lesser Antilles island arc. *Journal of Petrology* **21**, 743–799.

Atherton, M. P. (1999). Shape and intrusion style of the Coastal batholith, Peru. In: *4th International Symposium on Andean Geodynamics*, (extended abstract) 60–63.

Bachmann, O. & Dungan, M. A. (2002). Temperature-induced Al-zoning in hornblendes of the Fish Canyon magma, Colorado. *American Mineralogist* **87**, 1062–1076.

Baranov, B.V., Seliverstov, N.I., Murav'ev, A. V. & Muzurov, E. L. (1991). The Komandorsky Basin as a product of spreading behind a transform plate boundary. *Tectonophysics* **199**, 237–269.

Bateman, P. C. (1992). *Journal of Volcanology and Geothermal Research* **66**, 357–365.

Belousov, A. B., Belousova, M. & Voight, B. (1999). Multiple edifice failures, debris avalanches and associated eruptions in the Holocene history of Shiveluch volcano, Kamchatka, Russia. *Bulletin of Volcanology* **61**, 324–342.

Blundy, J. & Cashman, K. (2001). Ascent-driven crystallisation of dacite magmas at Mount St. Helens, 1980–1986. *Contributions to Mineralogy and Petrology* **140**, 631–650.

Blundy, J. & Cashman, K. (2005). Rapid decompression-driven crystallization recorded by melt inclusions from Mount St. Helens volcano. *Geology* **33**, 793–796.

Blundy, J., Cashman, K. & Humphreys, M. (2006). Magma heating by decompression-driven crystallisation beneath andesite volcanoes. *Nature* **443**, 76–80.

Blundy, J. D. & Sparks, R. S. J. (1992). Petrogenesis of mafic inclusions in granitoids of the Adamello Massif, Italy. *Journal of Petrology* **33**, 1039–1104.

Blundy, J. D. & Wood, B.J. (1991). Crystal-chemical controls on the partitioning of Sr and Ba between plagioclase feldspar, silicate melts and hydrothermal solutions. *Geochimica et Cosmochimica Acta* **55**, 193–209.

Bottinga, Y., Kudo, A. & Weill, D. (1966). Some observations on oscillatory zoning and crystallization of magmatic plagioclase. *American Mineralogist* **51**, 792–806.

Browne, B. L. & Gardner, J. E. (2002). Experimental calibration of amphibole breakdown rates in response to decompression and heating. *EOS Transactions, American Geophysical Union* **83**, F1464.

Buckley, V. J. E. (2003). Hornblende dehydration during magma decompression. Unpublished Ph.D. thesis, University of Bristol.

Calanchi, N., De Rosa, R., Mazzuoli, R., Rossi, P., Santacroce, R. & Ventura, G. (1993). Silicic magma entering a basaltic magma chamber: eruptive dynamics and magma mixing—an example from Salina (Aeolian islands, South Tyrrhenian Sea). *Bulletin of Volcanology* **55**, 504–522.

Candela, P. A. (1986). The evolution of aqueous vapour from silicate melts: effect on oxygen fugacity. *Geochimica et Cosmochimica Acta* **50**, 1205–1211.

Carroll, M. R. & Rutherford, M. J. (1985). Sulfide and sulfate saturation in hydrous silicate melts. *Journal of Geophysical Research* **90**, C601–C612.

Carroll, M. R. & Rutherford, M. J. (1988). Sulfur speciation in hydrous experimental glasses of varying oxidation state: results from measured wavelength shifts of sulfur X-rays. *American Mineralogist* **73**, 845–849.

Clemens, J. D., Petford, N. & Mawer, C. K. (1997). Ascent mechanisms of granitic magmas: causes and consequences. In: Holness, M. (ed.) *Deformation-enhanced fluid transport in the Earth's crust and mantle*. London: Chapman & Hall, pp. 144–171.

Clynne, M. A. (1999). A complex magma mixing origin for rocks erupted in 1915, Lassen Peak, California. *Journal of Petrology* **40**, 105–132.

Clynne, M. A. & Borg, L. E. (1997). Olivine and chromian spinel in primitive calc-alkaline and tholeiitic lavas from the southernmost Cascade Range, California: a reflection of relative fertility of the source. *Canadian Mineralogist* **35**(2), 453–472.

Couch, S., Sparks, R. S. J. & Carroll, M. R. (2001). Mineral disequilibrium in lavas explained by convective self-mixing in open magma chambers. *Nature* **411**, 1037–1039.

Czamanske, G. K. & Wones, D. R. (1973). Oxidation during magmatic differentiation, Finnmarka Complex, Oslo Area, Norway: Part 2, The mafic silicates. *Journal of Petrology* **14**, 349–380.

D'Lemos, R. S. (1996). Mixing between granitic and dioritic crystal mushes, Guernsey, Channel Islands, UK. *Lithos* **38**, 233–257.

Dirksen, O., Humphreys, M. C. S., Pletchov, P., Melnik, O., Demyanchuk, Y., Sparks, R. S. J. & Mahony, S. (2006). The 2001–2004 dome-forming eruption of Shiveluch Volcano, Kamchatka: observation, petrological investigation and numerical modelling. *Journal of Volcanology and Geothermal Research* , doi:10.1016/j.jvolgeores.2006.03.029.

Dungan, M. A. & Davidson, J. (2004). Partial assimilative recycling of the mafic plutonic roots of arc volcanoes: an example from the Chilean Andes. *Geology* **32**, 773–776.

Eichelberger, J. C. (1978). Andesitic volcanism and crustal evolution. *Nature* **275**, 21–27.

Eichelberger, J. C. (1980). Vesiculation of mafic magma during replenishment of silicic magma reservoirs. *Nature* **288**, 446–450.

Firstov, P. P., Gavrilov, V. A., Zhadnova, E. Yu. & Kiriyanov V. Yu. (1994). Onset of new extrusive eruption of Shiveluch in April 1993. *Volcanology and Seismology* **4–5**, 33–47 (in Russian).

Geist, E. L. & Scholl, D. W. (1994). Large-scale deformation related to the collision of the Aleutian arc with Kamchatka. *Tectonics* **13**, 538–560.

Gerlach, D. C. & Grove, T. L. (1982). Petrology of Medicine Lake Highland volcanics—characterization of end-memebers of magma mixing. *Contributions to Mineralogy and Petrology* **80**, 147–159.

Geschwind, C.-H. & Rutherford, M. J. (1995). Crystallization of microlites during magma ascent: the fluid mechanics of 1980–1986 eruption at Mount St Helens. *Bulletin of Volcanology* **57**, 356–370.

Gill, J. B. (1981). *Orogenic Andesites and Plate Tectonics*. Berlin: Springer.

Ginibre, C., Woerner, G. & Kronz, A. (2002). Minor- and trace-element zoning in plagioclase: implications for magma chamber proces at Parinacota volcano, northern Chile. *Contributions to Mineralogy and Petrology* **143**, 300–315.

Glazner, A. F., Bartley, J. M., Coleman, D. S., Gray, W. & Taylor, R. Z. (2004). Are plutons assembled over millions of years by amalgamation from small magma chambers? *GSA Today* **14**, 4–11.

Grove, T. L., Baker, M. B. & Kinzler, R. J. (1984). Coupled CaAl–NaSi diffusion in plagioclase feldspar: experiments and applications to cooling rate speedometry. *Geochimica et Cosmochimica Acta* **48**, 2113–2121.

Hammond, P. A. & Taylor, L.A. (1982). The ilmenite/titano-magnetite assemblage: kinetics of re-equilibration. *Earth and Planetary Science Letters* **61**, 143–150.

Hofmeister, A. M. & Rossman, G. R. (1984). Determination of Fe^{3+} and Fe^{2+} concentrations in feldspar by optical-absorption and electron-paramagnetic-resonance spectroscopy. *Physics and Chemistry of Minerals* **11**, 213–224.

Holland, T. & Blundy, J. D. (1994). Non-ideal interactions in calcic amphiboles and their bearing on amphibole–plagioclase thermometry. *Contributions to Mineralogy and Petrology* **116**, 433–447.

Holtz, F. & Johannes, W. (1994). Maximum and minimum water contents of granitic melts: implications for chemical and physical properties of ascending magmas. *Lithos* **32**, 149–159.

Holtz, F., Johannes, W., Tamic, N. & Behrens, H. (2001). Maximum and minimum water contents of granitic melts generated in the crust: a reevaluation and implications. *Lithos* **56**, 1–14.

Housh, T. B. & Luhr, J. F. (1991). Plagioclase–melt equilibria in hydrous systems. *American Mineralogist* **76**, 477–492.

Humphreys, M. C. S. (2006). Andesite petrogenesis and magmatic processes at Shiveluch Volcano, Kamchatka. Ph.D. thesis, University of Bristol.

Humphreys, M. C. S., Kearns, S. & Blundy, J. D. (2006). SIMS investigation of electron-beam damage to hydrous, rhyolitic glasses: implications for melt inclusion analysis. *American Mineralogist* **91**, 667–679.

Huppert, H. E., Sparks, R. S. J. & Turner, J. S. (1982). Effect of volatiles on mixing in calc-alkaline magma systems. *Nature* **297**, 554–557.

Jellinek, A. M., Kerr, R. C. & Griffiths, R. W. (1999). Mixing and compositional stratification produced by natural convection. 1. Experiments and their application to Earth's core and mantle. *Journal of Geophysical Research* **104**(B4), 7183–7201.

Johannes, W. & Holtz, F. (1996). *Petrogenesis and Experimental Petrology of Granitic Rocks*. Berlin: Springer.

John, B. E. & Blundy, J. D. (1993). Emplacement-related deformation of granitoid magmas, southern Adamello Massif, Italy. *Geological Society of America Bulletin*, **105**(12), 1517–1541.

Johnson, M. C. & Rutherford, M. J. (1989). Experimental calibration of the aluminium-in-hornblende geobarometer with application to Long Valley caldera (California) volcanic rocks. *Geology* **17**, 837–841.

Kawamoto, T. (1992). Dusty and honeycomb plagioclase—indicators of processes in the Uchino stratified magma chamber, Izu Peninsula, Japan. *Journal of Volcanology and Geothermal Research* **49**, 191–208.

Kouchi, A. & Sunagawa, I. (1985). A model for mixing basaltic and dacitic magmas as deduced from experimental data. *Contributions to Mineralogy and Petrology* **89**, 17–23.

Koyaguchi, T. (1985). Magma mixing in a volcanic conduit. *Journal of Volcanology and Geothermal Research* **25**, 365–369.

Leake, B. E. (1978). Nomenclature of amphiboles. *American Mineralogist* **63**, 1023–1052.

Lindsley, D. H. (1983). Pyroxene thermometry. *American Mineralogist* **68**, 477–493.

Liu, Y. & Comodi, P. (1993). Some aspects of the crystal-chemistry of apatites. *Mineralogical Magazine* **57**, 709–719.

Longerich, H. P., Jackson, S. E. & Günther, D. (1996). Laser ablation inductively coupled plasma mass spectrometric transient signal data acquisition and analyte concentration calculation. *Journal of Atomic Analytical Spectrometry* **11**, 899–904.

Longhi, J., Walker, D. & Hays, J. F. (1976). Fe and Mg in plagioclase. *Proceedings of the 7th Lunar Science Conference. Geochimica et Cosmochimica Acta Supplement*, 1281–1300.

Matthews, S. J., Jones, A. P. & Beard, A. D. (1994). Buffering of melt oxygen fugacity by sulphur redox reactions in calc-alkaline magmas. *Journal of the Geological Society, London* **151**, 815–823.

McBirney, A. R. (1980). Mixing and unmixing of magmas. *Journal of Volcanology and Geothermal Research* **7**, 357–371.

Melekestsev, I. V. *et al.* (1991). Shiveluch Volcano. In: Fedotov, S. A., Masurenkov & Yu, P. (eds) *Active Volcanoes of Kamchatka, Vol. 1.* Moscow: Nauka.

Melnik, O. & Sparks, R. S. J. (2005). Controls on conduit magma flow dynamics during lava dome building eruptions. *Journal of Geophysical Research* **110**, B02209, doi:10.1029/2004JB003183.

Menyailov, A. A. (1955). *Shiveluch Volcano, its Geological Structure, Composition and Eruptions. Transactions of the Volcanology Laboratory, USSR Academy of Sciences* **9**, 264 pp.

Miyashiro, A. (1974). Volcanic rock series in island arcs and active continental margins. *American Journal of Science* **274**, 321–355.

Murphy, M. D., Sparks, R. S. J., Barclay, J., Carroll, M. R., Lejeune, A. M., Brewer, T. S., Macdonald, R., Black, S. & Young, S. (1998). The role of magma mixing in triggering the current eruption at the Soufrière Hills volcano, Montserrat, West Indies. *Geophysical Research Letters* **25**, 3433–3436.

Murphy, M. D., Sparks, R. S. J., Barclay, J., Carroll, M. R. & Brewer, T. S. (2000). Remobilization of andesite magma by intrusion of mafic magma at the Soufrière Hills Volcano, Montserrat, West Indies. *Journal of Petrology* **41**, 21–42.

Nakada, S. & Motomura, Y. (1999). Petrology of the 1991–1995 eruption at Unzen: effusion pulsation and groundmass crystallization. *Journal of Volcanology and Geothermal Research* **89**, 173–196.

Nakamara, M. & Shimakita, S. (1998). Dissolution origin and syn-entrapment compositional change of melt inclusion in plagioclase. *Earth and Planetary Science Letters* **161**, 119–133.

Nash, W. P. & Crecraft, H. R. (1985). Partition coefficients for trace elements in silicic magmas. *Geochimica et Cosmochimica Acta* **49**, 2309–2322.

Nelson, S. T. & Montana, A. (1992). Sieve-textured plagioclase in volcanic rocks produced by rapid decompression. *American Mineralogist* **77**, 1242–1249.

Newman, S. & Lowenstern, J. B. (2002). VolatileCalc: a silicate melt–H_2O–CO_2 solution model written in Visual Basic for Excel. *Computers and Geosciences* **28**, 597–604.

Nishimura, K., Kawamoto, T., Kobayashi, T., Sugimoto, T. & Yamashita, S. (2005). Melt inclusion analysis of the Unzen 1991–1995 dacite: implications for crystallisation processes of dacite magma. *Bulletin of Volcanology* **67**, 648–662.

Parat, F. & Holtz, F. (2004). Sulfur partitioning between apatite and melt and effect of sulfur on apatite solubility at oxidizing conditions. *Contributions to Mineralogy and Petrology* **147**, 201–212.

Parat, F., Dungan, M. A. & Streck, M. J. (2002). Anhydrite, pyrrhotite, and sulfur-rich apatite: tracing the sulfur evolution of an Oligocene andesite (Eagle Mountain, CO, USA). *Lithos* **64**, 63–75.

Pearce, T. H. & Kolisnik, A. M. (1990). Observations of plagioclase zoning using interference imaging. *Earth-Science Reviews* **29**, 9–26.

Pearce, N. J. G., Perkins, W. T., Westgate, J. A., Gorton, M. P., Jackson, S. E., Neal, C. R. & Chenery, S. P. (1997). A compilation of new and published major and trace element data for NIST SRM 610 and NIST SRM 612 glass reference materials. *Geostandards Newsletter* **21**, 115–144.

Peng, G., Luhr, J. F. & McGee, J. J. (1997). Factors controlling sulfur concentrations in volcanic apatite. *American Mineralogist* **82**, 1210–1224.

Portnyagin, M., Hoernle, K., Avdeiko, G. & Hauff, F. (2005). Transition from arc to oceanic magmatism at the Kamchatka–Aleutian junction. *Geology* **33**(1), 25–28.

Pouchou, J. L. & Pichoir, F. (1984). 'PAP' (φ–ρ–z) correction procedure for improved quantitative microanalysis. In: Armstrong, J. T. (ed.) *Microbeam Analysis*. San Francisco, CA: San Francisco Press, pp. 104–106.

Putirka, K. D. (2005). Igneous thermometers and barometers based on plagioclase + liquid equilibria: tests of some existing models and new calibrations. *American Mineralogist* **90**, 336–346.

Pyle, D. M., Ivanovich, M. & Sparks, R. S. J. (1988). Magma–cumulate mixing identified by U–Th disequilibrium dating. *Nature* **331**, 157–159.

Raia, F. & Spera, F. J. (1997). Simulation for the growth and differentiation of continental crust. *Journal of Geophysical Research* **102**, 22629–22648.

Rutherford, M. J. & Devine, J. D. (2003). Magmatic conditions and magma ascent as indicated by hornblende phase equilibria and reactions in the 1995–2002 Soufrière Hills magma. *Journal of Petrology* **44**, 1433–1454.

Rutherford, M. J. & Hill, P. M. (1993). Magma ascent rates from amphibole breakdown: an experimental study applied to the 1980–1986 Mount St. Helens eruptions. *Journal of Geophysical Research* **98**, 19667–19685.

Sakuyama, M. (1984). Magma mixing and magma plumbing systems in island arcs. *Bulletin of Volcanology* **47**, 685–703.

Scaillet, B. & Evans, B. W. (1999). The 15 June 1991 eruption of Mount Pinatubo. I. Phase equilibria and pre-eruption P–T–$f$$O_2$–$f$$H_2O$ conditions of the dacite magma. *Journal of Petrology* **40**, 381–411.

Singer, B. S., Dungan, M. A. & Layne, G. D. (1995). Textures and Sr, Ba, Mg, Fe, K, and Ti compositional profiles in volcanic plagioclase: clues to the dynamics of calc-alkaline magma chambers. *American Mineralogist* **80**, 776–798.

Snyder, D. & Tait, S. (1996). Magma mixing by convective entrainment. *Nature* **379**, 529–531.

Sparks, R. S. J. & Marshall, L. A. (1986). Thermal and mechanical constraints on mixing between mafic and silicic magmas. *Journal of Volcanology and Geothermal Research* **29**, 99–124.

Sparks, R. S. J., Sigurdsson, H. & Wilson, L. (1977). Magma mixing—mechanism for triggering acid explosive eruptions. *Nature* **267**, 315–318.

Sparks, R. S. J., Murphy, M. D., Lejeune, A. M., Watts, R. B., Barclay, J. & Young, S. R. (2000). Control on the emplacement of the andesite lava dome of the Soufrière Hills Volcano, Montserrat by degassing-induced crystallization. *Terra Nova* **12**, 14–20.

Stormer, J. C. (1983). The effects of recalculation on estimates of temperature and oxygen fugacity from analyses of multicomponent iron titanium oxides. *American Mineralogist* **68**, 586–594.

Sugawara, T. (2000). Thermodynamic analysis of Fe and Mg partitioning between plagioclase and silicate liquid. *Contributions to Mineralogy and Petrologyz* **138**, 101–113.

Tiepolo, M., Zanetti, A., Oberti, R., Brumm, R., Foley, S. & Vannucci, R. (2003). Trace-element partitioning between synthetic potassic-richterites and silicate melts, and contrasts with the partitioning behaviour of pargasite and kaersutites. *European Journal of Mineralogy* **15**, 329–340.

Tischendorf, G., Förster, H.-J. & Gottsman, B. (2001). Minor- and trace-element composition of trioctahedral micas: a review. *Mineralogical Magazine* **65**, 249–276.

Tsuchiyama, A. (1985). Dissolution kinetics of plagioclase in the melt of the system diopside–albite–anorthite, and origin of dusty

plagioclase in andesites. *Contributions to Mineralogy and Petrology* **89**, 1–16.

Turner, S., George, R., Jerram, D. A., Carpenter, N. & Hawkesworth, C. (2003). Case studies of plagioclase growth and residence times in island arc lavas from Tonga and the Lesser Antilles, and a model to reconcile discordant age information. *Earth and Planetary Science Letters* **214**, 279–294.

Vance, J. A. (1965). Zoning in igneous plagioclase: patchy zoning. *Journal of Geology* **73**, 636–651.

van Lamoen, H. (1979). Coronas in olivine gabbros and iron ores from Susimaki and Riuttamaa, Finland. *Contributions to Mineralogy and Petrology* **68**, 259–268.

Venezky, D. Y. & Rutherford, M. J. (1999). Petrology and Fe–Ti oxide re-equilibration of the 1991 Mount Unzen mixed magma. *Journal of Volcanology and Geothermal Research* **89**, 213–230.

Wiebe, R. A. (1987). Rupture and inflation of a basic magma chamber by silicic liquid. *Nature* **326**, 69–71.

Wiebe, R. A. & Collins, W. J. (1998). Depositional features and stratigraphic sections in granitic plutons: implications for the emplacement and crystallization of granitic magma. *Journal of Structural Geology* **20**, 1273–1289.

Wilke, M. & Behrens, H. (1999). The dependence of the partitioning of iron and europium between plagioclase and hydrous tonalitic melt on oxygen fugacity. *Contributions to Mineralogy and Petrology* **137**, 102–114.

Wyllie, P. J., Cox, K. G. & Biggar, G. M. (1962). The habit of apatite in synthetic and igneous systems. *Journal of Petrology* **3**, 238–243.

Zharinov, N. A., Bogoyavlenskaya, G. E., Khubunaya, S. A., Demyanchuk & Yu, V. (1995). New eruptive cycle on Shiveluch Volcano—1980–1993. *Volcanology & Seismology* **1**, 20–28, (in Russian).